Chemistry–A European Journal

Research Article
doi.org/10.1002/chem.202401720

Chemistry Europe
European Chemical Societies Publishing

www.chemeurj.org

Photostimulated Anticancer Activity of Mitochondria Localized Rhenium(I) Tricarbonyl Complexes Bearing 1*H*-imidazo[4,5-*f*][1,10]phenanthroline Ligands Against MDA-MB-231 Cancer Cells

Binoy Kar[a] and Priyankar Paira*[a]

We have introduced Re(I) tricarbonyl complexes (**ReL1** - **ReL6**) $[Re(CO)_3(N\hat{}N)Cl]$ where N^N = extensive π conjugated imidazo-[4,5-f][1,10]-phenanthroline derivatives that helps in strong DNA intercalation, enhanced photophysical behavior, increase the $^3\pi$-π^* character of T_1 state for PDT and high value of lipophilicity for cell membrane penetration. These complexes exhibited prominent intraligand/ligand-centered (π-$\pi^*/^1$LC) absorption bands at λ 260–350 nm and relatively weak metal-to-ligand charge-transfer (^{1}MLCT) bands within the λ 350–550 nm range. Among the six synthesized complexes, $[(CO)_3Re^{I}Cl(K^2$-N,N-2-(4-(1-benzyl-1H-tetrazol-5-yl)phenyl)-1H-imidazo[4,5-f][1,10]phenanthroline] (**ReL6**) exhibited outstanding potency (IC_{50}~6 μM, PI > 9) under yellow light irradiation compared to dark conditions. Importantly, extremely lipophilic complex **ReL6** showed effective penetration through the cell membrane and localized primarily in mitochondria (Pearson's correlation coefficient, PCC = 0.918) of MDA-MB-231 cells. Complex **ReL6** exhibited more than 9 times higher photo-toxicity in normoxic and hypoxic environment of tumor by inducing $^1O_2$ generation (type II PDT), radical generation triggered by NADH oxidation (type I PDT). This complex is a promising candidate for TNBC treatment in hypoxic tumors, with efficacy comparable to photofrin and have demonstrated CO release ability under UV light irradiation.

1. Introduction

Since cancer is reckoned as the second main cause of death worldwide after cardiovascular disease (CVD), there is relentless research being done to find novel anticancer medications. The platinum-based complexes cisplatin, lobaplatin, oxaliplatin, and carboplatin are among the frontline anticancer drugs. Although they exhibited significant results in cellular apoptosis, they have serious adverse effects and have limited effectiveness against tumors that are resistant to platinum drugs. All-encompassing research has been conducted on organometallic and inorganic compounds as reasonable choices to pharmaceuticals derived from organic substances.[1,2] In this context, the promise of Ru(II/III) and Ir(III) complexes emerges from their reduced side effects and favorable characteristics. These include targeted actions on DNA or proteins, accumulation within various cellular organelles, amplified oxidative stress, photoactivation, improved cytotoxicity specifically against cancer cells, and disruption of the cellular redox balance.[3-5] Notably, several ruthenium complexes, such as NAMI-A, KP1019, KP1339, and TLD1433 have advanced into clinical trials.[6] In addition, in the realm of anticancer drug research, there has been a notable surge of interest in organometallic tricarbonyl rhenium(I) complexes and these compounds are being considered as promising alternatives to traditional agents like cisplatin and its congeners due to several potential applications and properties such as significant stokes shifts, prolonged emission states, tunable emission through ligand modifications, high quantum yields, ability to bind to proteins and DNA.[7–10] Initially, the diverse cell death mechanisms triggered by rhenium complexes, including paraptosis, apoptosis, and necroptosis, offer a potential solution to certain constraints associated with current medications.[11,12] Secondly, they find utility in photoactivatable therapy and photodynamic therapy (PDT) by employing CO-releasing mechanisms that can be activated through appropriate irradiation in tumor regions.[13,14] Additionally, Re tricarbonyl complexes play a role in bioimaging using fluorescence or vibration, aiding in visualizing cellular distribution and understanding the mechanism of action.[15]

Historically, cancer treatment has predominantly relied on conventional methods such as surgery, radiotherapy, and chemotherapy.[16] While contemporary research has introduced innovative therapeutic approaches like hormone-based therapy, stem cell therapy, and immunotherapy, photodynamic therapy (PDT) has emerged as a notable and well-established complementary or alternative approach in cancer treatment.[17,18] The development of noninvasive PDT aimed to mitigate the well-documented side effects associated with often non-selective chemotherapy. PDT involves the synergetic action of three components i.e. the utilization of light, a photosensitizer (PS), and cellular oxygen. The absorption of light by the photosensitizer (PS) generates a responsive excited state (PS*) capable of engaging in either electron transfer (Type I) or energy transfer (Type II) with the ground-state molecular oxygen, generating reactive oxygen species (ROS) like singlet

[a] *B. Kar, P. Paira*
Department of Chemistry, School of Advanced Sciences, Vellore Institute of Technology, Vellore, Tamil Nadu 632014, India
E-mail: priyankar.paira@vit.ac.in

Supporting information for this article is available on the WWW under https://doi.org/10.1002/chem.202401720

oxygen ($^1O_2$), hydroxyl radical ($HO^•$), superoxide radical ($O_2^{•-}$), and hydrogen peroxide (H_2O_2).[19,20] The lifetime of $^1O_2$ in a biological environment is very short, the damage to unaffected cell proximity to the irradiation zone will be insignificant. A desirable photosensitizer (PS) possesses the capability to absorb light within the therapeutic range (600-900 nm), an optimal energy level for the triplet state, and a sufficiently prolonged triplet state lifetime, facilitating the generation of reactive oxygen species.[21,22]

Nowadays, we observe a notable scarcity of approved PSs for such PDT treatments. The majority of these PSs rely on porphyrin and porphyrinoid structures, encompassing chlorins, bacteriochlorin's, many organic compounds containing C^N bidentate, N^N bidentate, tridentate ligand, and similar configurations.[23–25] Challenges like short excited state lifetime, insufficient selectivity, low water solubility, potential toxicity to healthy tissues, and skin sensitivity associated with certain photosensitizers pose difficulties to the clinical adoption of various photodynamic therapeutic strategies.[22,26] The approaches to solve these problems are (i) increasing the energy gap between the nonradioactive d-d state (MC) and ^{3}MLCT; (ii) increasing the $^3\pi$-π^* character to increase the T_1 lifetime. The ligands with extended π-systems lower the energy of ligand centered (LC) $^3\pi$-π^* state to below, or close to, that of the ^{3}MLCT state, extraordinarily accumulating the $^3\pi$-π^* character of T_1 state.

In recent years, many research teams have endeavored to address these concerns and produce new classes of PSs. In this category, recently, rhenium(I) tricarbonyl complexes have garnered attention as viable contenders for PDT because of their varied photophysical and biochemical characteristics, high photostability, and adaptability in terms of biocompatibility, which can be fine-tuned by altering the ligands.[27,28] Also, tricarbonylrhenium(I) complexes featuring N^N bidentate ligands also emerge as highly promising candidates for serving as "photo-activated CO-releasing molecules" (photoCORMs) with potential therapeutic applications. In addition to their role in CO release, these complexes can serve as luminescent indicators, aiding in the identification and evaluation of the intracellular photochemical release of CO, both terms of location and magnitude.[29] In these complexes, carbon monoxide (CO) release is commonly initiated through ligand-substitution reactions in aqueous solutions, an alternative approach explores the light-induced liberation of carbon monoxide from initially dark stable carbonyl complexes. Specifically, tricarbonyl rhenium complexes have been demonstrated to release CO under UV radiation and display cytotoxic effects against cancer cells, remaining inactive even after extended exposure in the absence of light.[13,29-31]

Taking these factors into account, our endeavor in this research was to formulate new PDT active compounds that might possess the capacity to surmount common challenges. In this context, we have designed and synthesized six organometallics Re(I) complexes (**ReL1**-**ReL6**) $[Re(CO)_3(N^N)Cl]$ where N^N = extensive π conjugated imidazo-[4,5-f][1,10]-phenanthroline derivatives. The introduction of (imidazo[4,5-f][1,10]phenanthrolin-2-yl)phenol as an extensively flat N^N chelating ligand results in strong DNA intercalation, enhances photophysical behavior, increases the $^3\pi$-π^* character of T_1 state and high value of lipophilicity.[32,33] The labile chlorine and CO group enhance the covalent interaction with DNA and facilitate interactions with other biomolecules such as human serum albumin (HSA), and glutathione (GSH).[34,35] The strong lipophilic rhenium component is anticipated to enhance both the efficiency of cellular uptake and the property of targeting mitochondria. After well characterization and purification of all these complexes, we performed photophysical characterization to evaluate their emission quantum yield and phototoxic screening against triple-negative human breast cell line MDA-MB-231 which demonstrated complex **ReL6** as the best potential compound. Subsequently, we conducted thorough investigations with complex **ReL6**, such as binding studies with DNA, proteins, and biomolecules, as well as studies on singlet oxygen and ROS generation, along with colocalization assessments and theoretical analysis. The CO release attributes under light which have the potential to trigger an additional cytotoxic effect, were also investigated using electronic absorption and emission spectroscopy, and Fourier transform infrared (FT-IR) techniques.

2. Results and Discussion

Synthesis and Characterization: The preparation of **L5** and **L6** involves a multi-step procedure, whereas the syntheses of **L1**-**L4** follow a one-step pathway. The ivory white compound **5** was synthesized by dissolving a mixture of 4-bromobenzaldehyde (1 equiv.), 4-biphenyl boronic acid (1 equiv.), tetrakis(triphenylphosphine)palladium(0), and K_2CO_3 (5 equiv.) in toluene under reflux for 4 h. To prepare white-colored compound **6**, in the first step (preparation of tetrazole **6′**), 4-formylbenzonitrile and sodium azide (excess) were liquefied in dimethylformamide (DMF), and treated in the presence of copper iodide (CuI) at 120 °C for 30 h whereas, in the second step (formation of compound **6**), we treated tetrazole **6′** (1 equiv.) with benzyl bromide (1.1 equiv.) in the presence of K_2CO_3 in DMF at 0 °C until the conversion was finished. The 1H-imidazo[4,5-f][1,10]phenanthrolin-2-yl)phenol ligands, denoted as **L1**-**L6**, were synthesized by reacting an equimolar mixture of 1,10-phenanthroline-5,6-dione and different derivatives of benzaldehyde (**1**-**6**) in the presence of ammonium acetate in glacial acetic acid, as illustrated in Scheme 1. The ligands (**L1**-**L6**) underwent complete characterization through ^{1}H and ^{13}C NMR, FT-IR, and ESI-HRMS analyses, while their purity was verified using elemental analysis. Then, 1 equiv. of pentacarbonylchlororhenium(I) and 1.1 equiv. of the previously prepared ligand (**L1**-**L6**) were dissolved in toluene and was then refluxed over the course of 6 h to prepare tricarbonylrhenium(I) complexes in high yield. The characterization of the metal complexes was done by ^{1}H and ^{13}C NMR spectroscopy, FT-IR spectroscopy, and ESI-HRMS. Elemental analysis was employed to confirm the purity of the complexes. In the ^{1}H NMR spectra of the metal complexes, the ligand proton peaks are observed to shift downfield in comparison to the free ligand, indicating

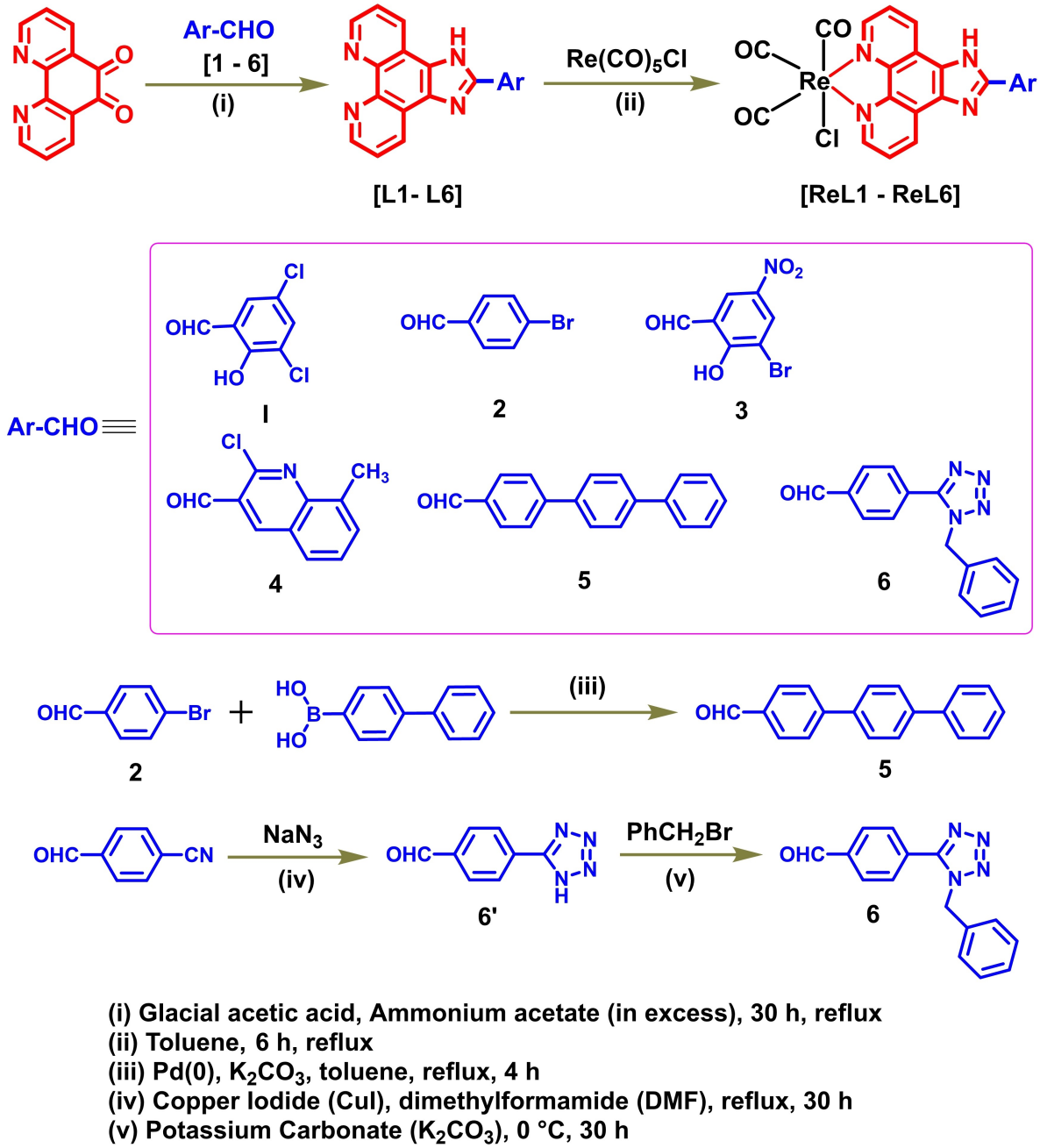

Scheme 1. Schematic representation for the formation of ligands (N^N) and $[Re^{I}(CO)_3(N^N)Cl]$ complexes.

coordination with the Re center. In **ReL6** (considered arbitrarily for discussion), ligand proton peaks are observed at δ 6.06 to 9.38 ppm whereas at δ 6.04 to 9.02 ppm in the free ligand **L6**. The peaks corresponding to the ligand are detected in the range of δ 56.8 to 164.4 ppm, and peaks attributed to carbonyl carbon are identified at δ 190.6 to 198.3 ppm in the ^{13}C NMR spectrum. Further confirmation of the complex formation was supported by the FT-IR spectrum, where the characteristic peaks of CO stretching frequencies at 2021.57 cm^{-1} and 1899.01 cm^{-1} were observed. In the ESI-HRMS analysis of complex **ReL6**, the observed m/z value of 766.1305 for $[M–Cl+CH_3CN]^+$ precisely corresponded to the calculated m/z value of 766.1325, confirming the metal complex formation. Likewise, all other complexes are well characterized by NMR, Mass and IR spectroscopy.

Theoretical Calculations: A computational study was also performed on the most potent complex **ReL6** to explore the photophysical characteristics. In this study, we employed Density Functional Theory (DFT) calculations to derive the energy-minimized three-dimensional structure of the analyzed complex. Our approach involved utilizing computational methods to elucidate the molecular geometry of the complex and optimize its energy state for further analysis of its properties. Theoretical calculations were conducted using the B3LYP exchange-correlation function. The energy-minimized opti-

mized structure of the complex unveiled specific bond lengths: 1.9243 Å for Re–C, 2.5468 Å for Re–Cl, and 2.1771 Å for Re–N. The structural geometry of complex **ReL6** was identified as a distorted octahedron with a C_1 point group, as evidenced by angles such as N–Re–Cl (82.66°), N–Re–C (93.48°), C_{axial}–Re–Cl (175.50°), $C_{equatorial}$–Re–Cl (91.51°), and C_{axial}–Re–$C_{equatorial}$ (91.75°). Furthermore, the HOMO-LUMO energy gap was computed to be 2.7935 eV, providing valuable information about the electronic characteristics of the complex. Examining the distribution of electron density revealed that the HOMO orbital predominantly localized over the Re-center and CO molecules, whereas the electron density of the LUMO was concentrated on the bidentate ligand (Figure 1). TD-DFT calculations anticipated two bands in the UV-visible spectra, aligning with experimental findings. The UV band was assigned to the ILCT transition from HOMO-3 to LUMO + 1, while the visible band originated from the MLCT transition between HOMO-1 and LUMO (Figure S1).

Electronic Absorption (UV-visible) and Emission Study: A majority of Re(I) tricarbonyl complexes exhibit prolonged phosphorescence, significant Stokes shifts, and elevated quantum yields, providing advantages for intracellular sensing and bioimaging.[36] Various electronic states, encompassing configurations like ligand-field (d-d*) or metal-centered (MC), intraligand (π-π*, IL), and charge-transfer (CT), are employed to elucidate the electronic UV-vis absorption spectra of metal complexes.[37] To underscore the cellular imaging attributes of the prepared complexes, investigations involving absorption (UV-visible) and emission were carried out in a 10% DMSO-water (1:9, v/v). Rhenium complexes (**ReL1**-**ReL6**) exhibited prominent absorption peaks in the range of λ 260-350 nm, which are ascribed to intraligand/ligand-centered (π-π*/ ^{1}LC) transitions. Additionally, there were relatively weak bands within the λ 350-550 nm range, associated with a metal-to-ligand charge-transfer (^{1}MLCT) process (Figure S2). We observed the experimental results are moderately correlated with the experimental results. The emission spectra of these complexes were observed in the range of λems 320-480 nm under π - π* excitation, and under MLCT excitation, they occurred at λems 500-750 nm (Table 1, Figure S2). The quantum yields (Φ_f) of these complexes were determined using the emission spectral data, offering insights for applications in photocytotoxicity and cellular imaging. It was apparent that all the compounds displayed significant fluorescence, exhibiting a high Φ_f value of approximately 0.22-0.51. The Φ_f value of complex **ReL6** reached the highest value at 0.508 among them (Equation (i), Table 1).

Lipophilicity (log *P*), Cellular Uptake, Solubility, and Conductivity Study: The cellular uptake and anticancer mechanisms of a compound are influenced by its lipophilicity (log *P*) and hydrophilic nature. The partition coefficient (log *P*) is an indicator of how a compound, in its ionized state, distributes between organic and water phases, which serves as a suitable estimation of physiological conditions.[38,39] Considering this, we assessed the lipophilicity of these complexes by determining the log *P* value in the n-Octanol-water mixture using a shake-flask method. The acquired experimental log $P_{o/w}$ values for these complexes ranged from 0.61 ± 0.02 to 1.34 ± 0.04, indicating their hydrophobic characteristics (Table 2). Among them, complex **ReL6** exhibited the highest log $P_{o/w}$ value of 1.34 ± 0.04 because of the presence of hydrophobic π-extensive aromatic group. The order of lipophilicity of the synthesized complexes were followed as **ReL6** > **ReL5** > **ReL4** > **ReL2** > **ReL1** > **ReL3**. In general, the log $P_{o/w}$ values of the synthesized complexes line

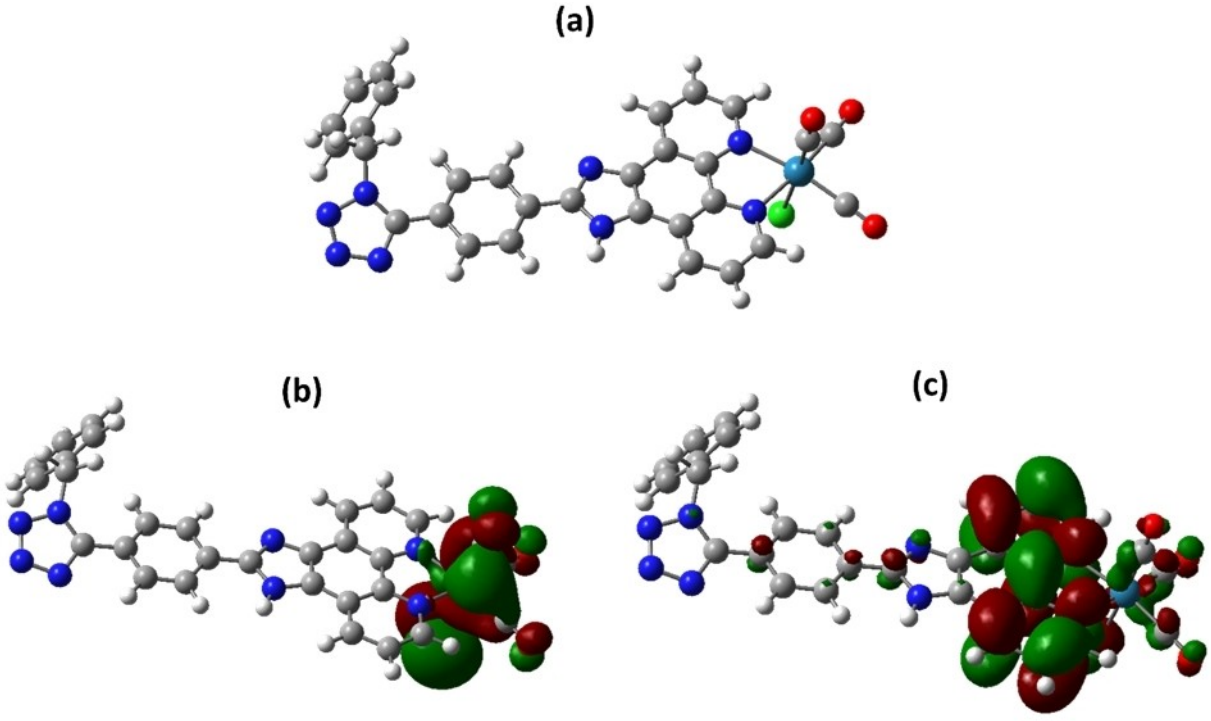

Figure 1. (**a**) Optimized structure of the complex **ReL6**, (**b**) HOMO electron density distribution (ISO = 0.02), (**c**) LUMO electron density distribution (ISO = 0.02).

Table 1. Photophysical profile of all the synthesized complexes (**ReL1-ReL6**).

Samples	λ_a(nm)[a]		λ_f (nm)[b]		Stoke's shift		O.D[c]	ε[d]	(ϕ_f)[e]
	π-π*	MLCT	π-π*	MLCT	π-π*	MLCT			
ReL1	283	428	375	593	92	165	0.48	15900	0.217
ReL2	288	427	360	589	72	162	0.47	15533	0.421
ReL3	281	430	344	591	63	161	0.32	10633	0.334
ReL4	276	420	352	518	76	98	0.31	10466	0.295
ReL5	270	418	386	570	116	152	0.28	9300	0.315
ReL6	297	438	391	591	94	153	0.38	12833	0.508
Quinine Sulphate	350		452		102		0.26	8000	0.546

[a] Absorption wavelength maxima. [b] Emission wavelength maxima. [c] Optical density. [d] Extinction coefficient($M^{-1}cm^{-1}$). [e] Quantum yield.

Table 2. Table for lipophilicity, cellular uptake, and conductivity study of all the complexes (**ReL1-ReL6**).

Samples		ReL1	ReL2	ReL3	ReL4	ReL5	ReL6
logPo/w[a]		0.78 ± 0.03	0.82 ± 0.04	0.61 ± 0.02	0.93 ± 0.05	1.18 ± 0.03	1.34 ± 0.04
Cellular uptake (pmole/10^6 cells)	**MDA-MB −231**	650 ± 8.2	700 ± 12.5	580 ± 11.4	800 ± 14.0	870 ± 10.2	920 ± 12.8
	MRC-5	119 ± 5.6	120 ± 7.2	116 ± 8.5	140 ± 6.5	180 ± 7.5	220 ± 6.4
■M (S.m^2. mol^{-1})[b]	**DMSO (±0.5)**	12.6	11.1	10.2	10.9	8.6	9.8
	10% DMSO (±1)	35	28	31	33	25	29

[a] n-Octanol/water partition coefficient. [b] Conductance in DMSO and 10% aqueous DMSO.

up favorably with those of other Re(I) tricarbonyl compounds described in the literature.[40] As cellular uptake is one of the key determinants of antitumor activity, the cellular accumulation of the synthesized Re(I) complexes were determined by measuring intracellular metal content using Inductively Coupled Plasma Mass Spectrometry (ICP-MS). MDA-MB-231 Cells were preserved with 4 μM complexes for 6 h and garnered, and total metal content was quantified by ICP-MS. As presented in Figure 2, the order of cancer cell accumulations (metal per 10^6 MDA-MB-231 cells) were followed similarly with the log $P_{o/w}$ values.

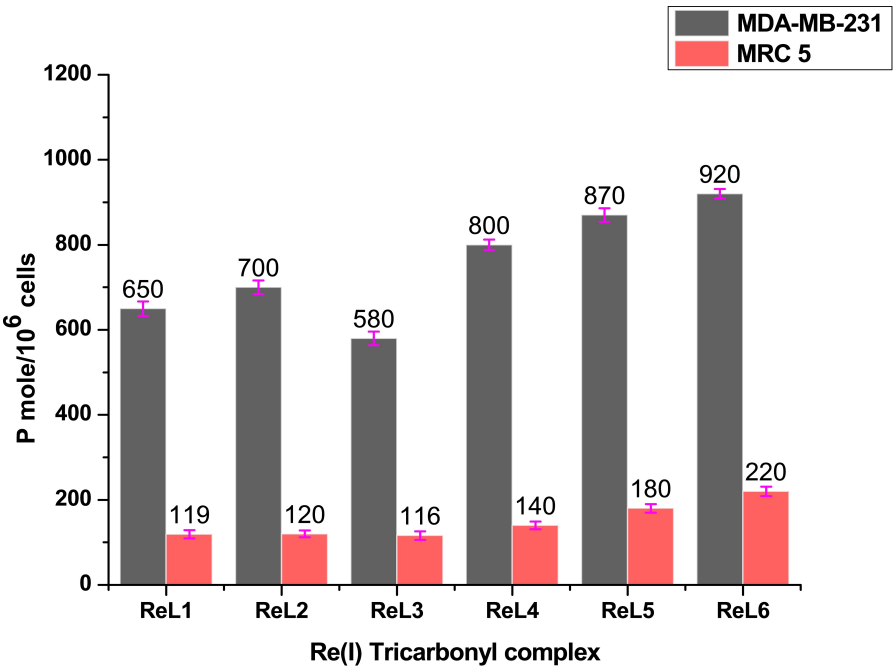

Figure 2. Cellular uptake of complexes (**ReL1-ReL6**) in MDA-MB-231 and MRC-5 cells. Data reflect the average ± SD of two independent experiments each performed in triplicate.

Subsequently, we compared the cellular uptake of synthesized Re(I) complexes in non-cancerous MRC-5 cells to know the effect of cellular accumulation on cancer cell selectivity. Eventually, all these complexes displayed similar uptake tendencies in normal cells, but uptake was much lower than cancer cells. The solubility of all these complexes was assessed through a diverse range of solvents. The complexes exhibited outstanding solubility in dimethyl sulfoxide, acetonitrile, and dimethylformamide while demonstrating fair solubility in water, ethanol, and methanol. The complexes displayed molar conductance values of approximately 8-15 $S.m^2 mol^{-1}$ in pure DMSO and in the range of 25-35 $S.m^2 mol^{-1}$ in 10% aqueous DMSO (Table 2). These results indicate their non-electrolytic behavior in DMSO and an electrolytic nature with a 1:1 ratio in an aqueous medium, attributed to the dissociation of the chloride ligand.[32,33,41]

Stability Study: Compounds capable of creating aqua complexes within cellular environments are indicated to involve in interactions with DNA base pairs through a covalent mode of action. To ascertain the dissociation rate of the complex **ReL6**, the stability was investigated through UV-visible spectroscopy. This analysis was carried out in a 5% DMSO-PBS (1:19, v/v) solution, with a pH of 7.4, as well as in a 5% DMSO-DMEM solution, a commonly utilized culture medium containing miscellaneous biological nucleophiles like amino acids, glucose, and nucleotides, along with elevated concentrations of salts, both performed at room temperature. The absorption spectra of the complex **ReL6** exhibited a negligible decrease of absorbance over 30 h duration in the absence of light, suggesting excellent stability in these media (Figure S3). Furthermore, a study on the stability of the complex **ReL6** was conducted in 2:3 (v/v) DMSO-d_6:10 mM PBS solution (pD = 7.4) (Figure S4) and 2:3 (v/v) DMSO-d_6:D_2O with 10 mM DMEM solution, utilizing ^{1}H NMR spectroscopy, recorded at various time intervals (0-30 h) at 37 °C (Figure S5). Nevertheless, no significant changes in NMR spectra are the indications of excellent stability of the complex **ReL6** reported from UV-visible absorption spectroscopy previously.

Effect of Kinetic Lability on Reactivity towards Biomolecules (GSH and NAC): A primary objective behind maintaining the labile –Cl with metal in the rhenium(I) tricarbonyl complexes was to expedite the covalent interaction rate with biomolecules containing nitrogen (N) and sulfur (S), such as guanine, adenine, ct-DNA, GSH, N-acetyl cysteine, and proteins. The investigation into the interaction between complex **ReL6**, recognized as the most potent among the compounds, and pertinent biomolecules (GSH, NAC) was conducted through ESI-HRMS and ^{1}H NMR spectroscopy (Figure 3). This approach aimed to gain deeper insights into the underlying mechanisms contributing to the *in vitro* anticancer activity exhibited by the rhenium complexes. For the ^{1}H NMR study, a mixture of complex **ReL6** and respective biomolecules (1:3) was prepared in DMSO-d_6/D_2O (2:1, v/v) at 37 °C, and the spectrum was recorded at several time intervals over 24 h. The implementation of time-dependent ^{1}H NMR measurements led to the observation of distinct changes in NMR signals, suggesting the formation of a novel covalent complex adducts (Figure 3, Figure S6, and Figure S7). This observation was further confirmed by the ESI-HRMS study after a 24 h reaction of complex **ReL6** with NAC and GSH respectively (1:3) in methanol. The m/z values of 885.6244 and 1032.2177 are indicating the formation of **ReL6**-NAC and **ReL6**-GSH adducts respectively (Figure 3, Figure S8, and Figure S9). This study also revealed that the conversion rate of **ReL6**-NAC formation is slightly higher than the **ReL6**-GSH formation depending on the size of biomolecules.

Oxidation and Reduction property of the complex by Cyclic Voltammetry: Given the pivotal role redox processes often play in influencing the anticancer properties of metal-based drug candidates, an examination of the electrochemical features of the compound **ReL6** was carried out through cyclic voltammetry (CV) in acetonitrile (CH_3CN), utilizing a 0.1 M solution of tetrabutylammonium perchlorate (TBAP) as the supporting electrolyte to assess the redox traits of the metal in the Re(I) complex. Figure S10 displays the acquired CV features, providing insights into the redox behavior of the complex. The quasi-reversible anodic peak identified at 1.54 V (I) in the case of complex **ReL6** was associated with the metal-centric oxidation process from Re^{1+} to Re^{2+}.[42] Additionally, the quasi-reversible anodic peak at 2.46 V (II) was ascribed to the oxidation of chloride ions. The other cathodic peaks observed at 1.16 V (III), −1.15 V (IV), and −1.63 V (V) for complex **ReL6** were related to the ligand-centric reduction processes. Moreover, in the case of complex **ReL6**, there is an additional reduction wave at −1.63 V, confirming the presence of a Re^I/Re^0 redox couple.[42,43] This behavior aligns with observations made in previous studies involving tricarbonyl Re(I) complexes incorporating different diimine derivatives. Significantly, it is worth noting that all these reduction events occur at potentials beyond the biologically relevant range.[44] Despite being outside this range, the recorded reduction potentials provide valuable insights into the electronic characteristics of these complexes. As expected, these potentials align with the electron-donating properties of the diimine ligands.

Molecular Docking and Molecular Dynamics Study: Detailed molecular docking experiments were conducted to investigate the binding modes and affinity of the studied complex **ReL6** with Human Serum Albumin (HSA) and DNA. Using the Autodock 4.2 computational program with the Lamarckian genetic algorithm (LGA), valuable insights were obtained through meticulous molecular docking experiments. Notably, the crystal structures of DNA (PDB ID: 1BNA) and HSA (PDB ID: 1AO6) sourced from the Protein Data Bank underwent a comprehensive protein preparation process. This process included the removal of water molecules, the addition of polar hydrogens, and the computation of Gesteiger charges, ensuring a robust foundation for subsequent analyses. Given the specific focus on DNA as a pivotal target for anticancer drugs, molecular docking study of the complex **ReL6** with DNA was conducted to elucidate its binding affinity. The obtained outcomes, indicating a binding energy of −16.02 kcal/mol and an inhibition constant of 1.81 pM, underscored the remarkable binding capability of the metal complex with DNA (Figure 4, Table S1). The molecular interactions that contribute to this

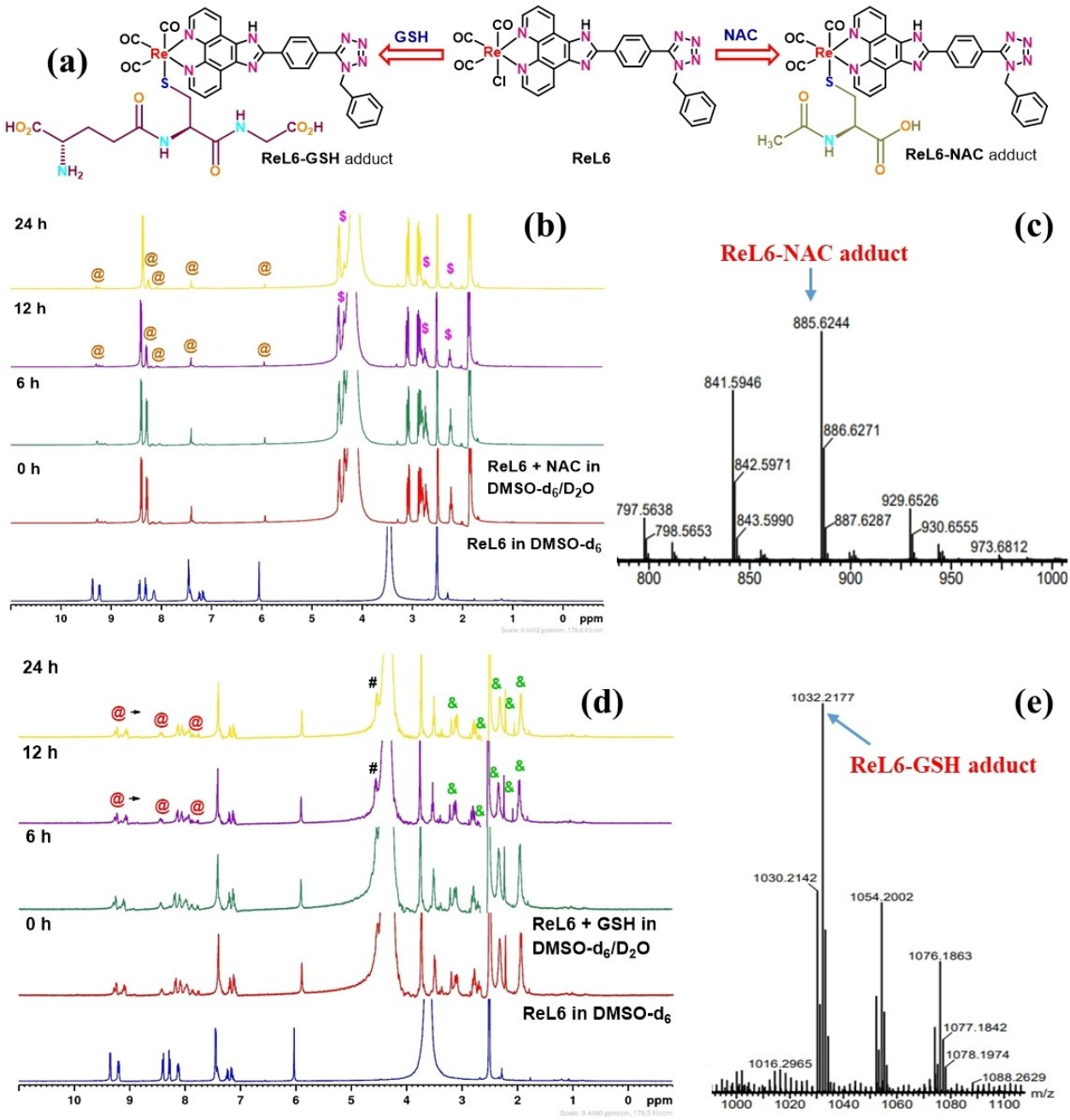

Figure 3. (a) Formation of adducts (**ReL6-NAC** and **ReL6-GSH**) with NAC and GSH through covalent interaction of complex **ReL6**. (b) Time-dependent ^{1}H NMR spectra of a mixture of complex **ReL6** and NAC (1 : 3) prepared in DMSO-d_6/D_2O (2/1, v/v) at 37 °C. (c) ESI-HRMS spectrum of a mixture of complex **ReL6** and NAC (1 : 3) prepared in MeOH after 24 h stirring at r.t. (d) Time-dependent ^{1}H NMR spectra of a mixture of complex **ReL6** and GSH (1 : 3) prepared in DMSO-d_6/D_2O (2/1, v/v) at 37 °C. (e) ESI-HRMS spectrum of a mixture of complex **ReL6** and GSH (1 : 3) prepared in MeOH after 24 h stirring at r.t. Full ESI-HRMS spectra are in supporting information.

enhanced affinity were carefully outlined, highlighting the creation of eight hydrogen bonds with T7, T20, G22, A6, T8, T19, A18, and C9 residues of DNA, where the complex effectively acted as both a donor and an acceptor. Moreover, the sophisticated binding profile was further enriched by electrostatic interaction with T7 residues.

The molecular docking of complex **ReL6** with HSA unveiled a binding energy of −13.89 kcal/mol and an inhibition constant of 66.27 pM, confirming the exceptional binding capacity of the complex with HSA (Figure 5, Table S1). The detailed molecular interactions contributing to this sharp binding affinity were elucidated, encompassing five hydrogen bonds with LEU115, LYS190, ARG186, LYS519, and SER517 residues, where the complex functioned as both a donor and an acceptor. Additionally, the complex binding profile was characterized by nine hydrophobic π-alkyl interactions with LYS137, ALA126, PRO118, MET123, ARG117, and LEU115 residues, along with three

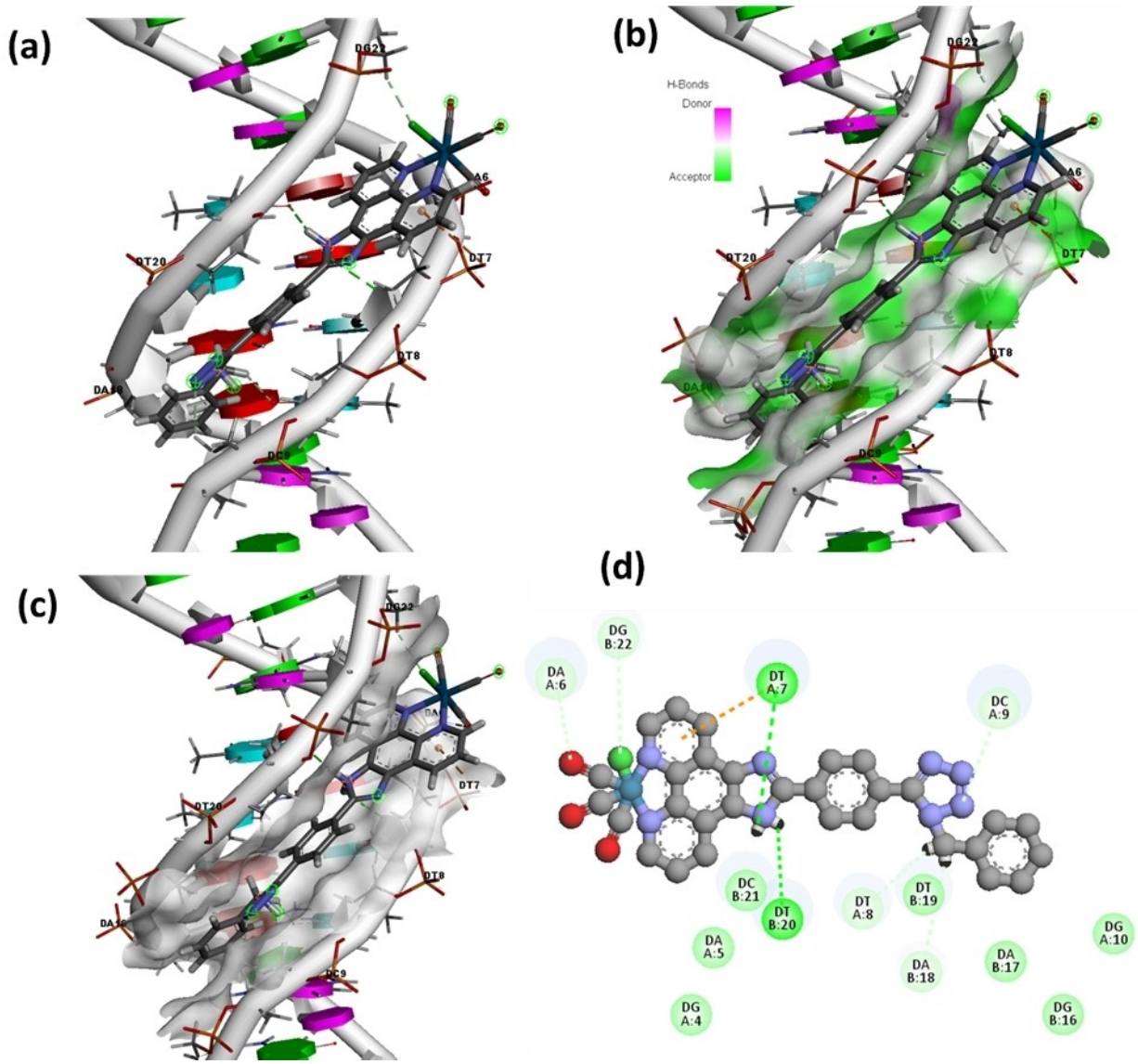

Figure 4. (a) The best dock pose of the complex **ReL6** exhibiting all the interactions between complex and DNA residues. **(b)** The best dock pose for exhibiting hydrogen bonding interactions between complex and DNA residues. **(c)** The best dock pose for exhibiting hydrophobic interactions between complex and DNA residues. **(d)** Schematic 2D diagram of the DNA-complex interaction.

electrostatic interactions involving ARG185 and ARG117 residues.

To investigate the stability of ligand-protein interactions derived from the docking outcomes, Molecular Dynamics (MD) simulations were performed for the optimal docking pose of the complex **ReL6** with HSA. The simulation results were influenced by various intricate factors, such as the conformation of a complex, the presence of water molecules, ions, cofactors, complex protonation, conformational changes, and solvent entropy, all of which were carefully considered. The subsequent MD simulation revealed robust stereochemical geometry of residues in the ultimate structure, and the RMSD plot indicated initial fluctuations within the first 10 ns, succeeded by a trend toward stabilization. The observed stabilization, as depicted in the RMSD plot, emphasized the sustained stability of the HSA complex, supporting the molecular interactions outlined during the docking studies. A detailed analysis of the contact residues unveiled a comprehensive network involving 18 specific residues, thereby providing additional affirmation of the robustness and accuracy of the docking results (Figure 6).[45]

DNA Binding Assay by UV-visible Study: UV-vis absorption spectroscopy is widely used to assess the interaction between molecules and ct-DNA through the formation of complexes. Typically, alterations in absorbance and/or shifts in peak positions are detected when small molecules interact with DNA to create a complex. Metal complexes exhibit two distinct binding modes with DNA: covalent and noncovalent interactions, encompassing intercalation, groove binding, and electrostatic interactions. To validate the interaction of complex **ReL6** with DNA, the absorption spectrum of the compound was examined in the presence of varying concentrations of ct-DNA within the 280–600 nm range. As the concentration of ct-DNA

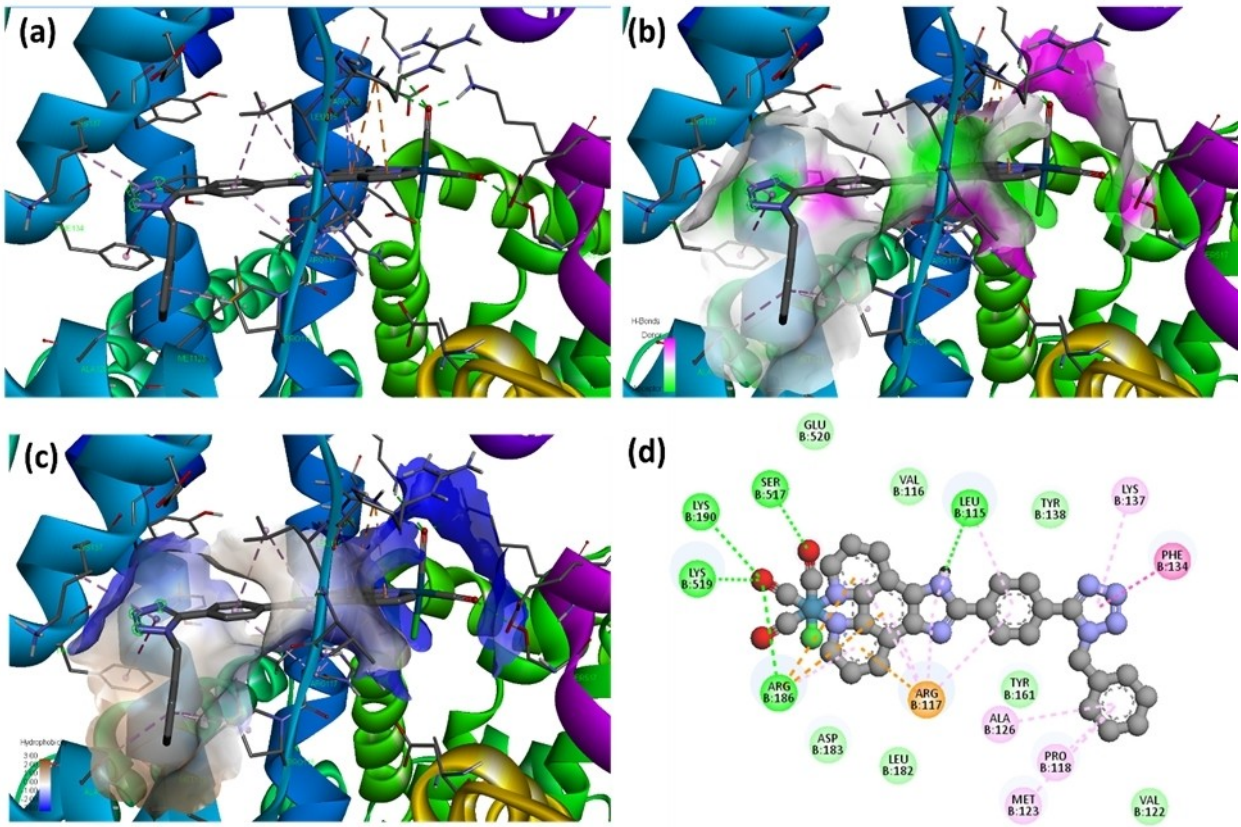

Figure 5. (a) The best dock pose of the complex **ReL6** exhibiting all the interactions between complex and HSA protein residues. **(b)** The best dock pose for exhibiting hydrogen bonding interactions between complex and HSA residues. **(c)** The best dock pose for exhibiting hydrophobic interactions between complex and HSA residues. **(d)** Schematic 2D diagram of the protein-complex interaction.

increased, the absorbance spectrum of the complex **ReL6** exhibited a hypochromicity of 39% for the peak at 298 nm and an isosbestic point was observed at 284 nm, along with a 2 nm hypsochromic shift in the peak at 298 nm. This spectral pattern is commonly associated with the intercalation as well as an electrostatic mode of the molecule with the DNA base pairs (Figure S11). The intrinsic binding constant (k_b) for the complex **ReL6** was determined as 4.4×10^5 M^{-1} (Equation (ii), Table 3, and Figure S11) which is of a similar magnitude to that of EtBr-DNA (7×10^5 M^{-1}).[4,32,33] The interaction of complexes with nucleobases like guanine and adenine base was observed using UV-visible spectroscopy. The spectral variations of these complexes, as the concentration of nucleobase increased, provided evidence that the complexes effectively form covalent bonds with DNA base pairs (Figure S12).[46,47]

Ethidium Bromide (EtBr) Displacement Assay: To examine the mechanism of interaction between the metal complex and DNA, complex **ReL6** was further subjected to an Ethidium Bromide (EtBr) displacement assay using fluorescence spectroscopy. EtBr exhibits intense fluorescence when intercalated with DNA base pairs, and this fluorescence may be diminished when another scaffold replaces EtBr and subsequently binds to the same DNA site.[47] A solution containing EtBr bound to ct-DNA displayed a strong fluorescence peak at 600 nm when excited at 485 nm. However, this fluorescence peak was diminished upon incubation with increasing concentrations of the complex **ReL6** (Figure S13). The calculated apparent binding constant (K_{app}) for complex **ReL6** was determined to be 2.28×10^6 M^{-1} using equation (iii). The Stern-Volmer quenching constant (K_{SV}) was computed from Equation (iv) as 0.349×10^6 M^{-1} for complex **ReL6**. The notable shift in spectral band position (hypochrom-

Table 3. Binding parameters for the interaction of complex **ReL6** with ct-DNA.

Complex	λ_{max} [nm]	Change in absorbance	[a] $\Delta\varepsilon$ (%)	[b] K_b ($\times10^6$ M^{-1})	[c] K_{SV} ($\times10^6$ M^{-1})	[d] K_{app} ($\times10^6$ M^{-1})
ReL6	298	Hypochromism	39	0.44 ± 0.03	0.349 ± 0.06	2.28 ± 0.25

[a] $\Delta\varepsilon$, percentage of hypochromism. [b] k_b, intrinsic DNA binding constant from UV-vis absorption titration. [c] K_{SV}, Stern-Volmer quenching constant. [d] K_{app}, apparent DNA binding constant from competitive displacement.

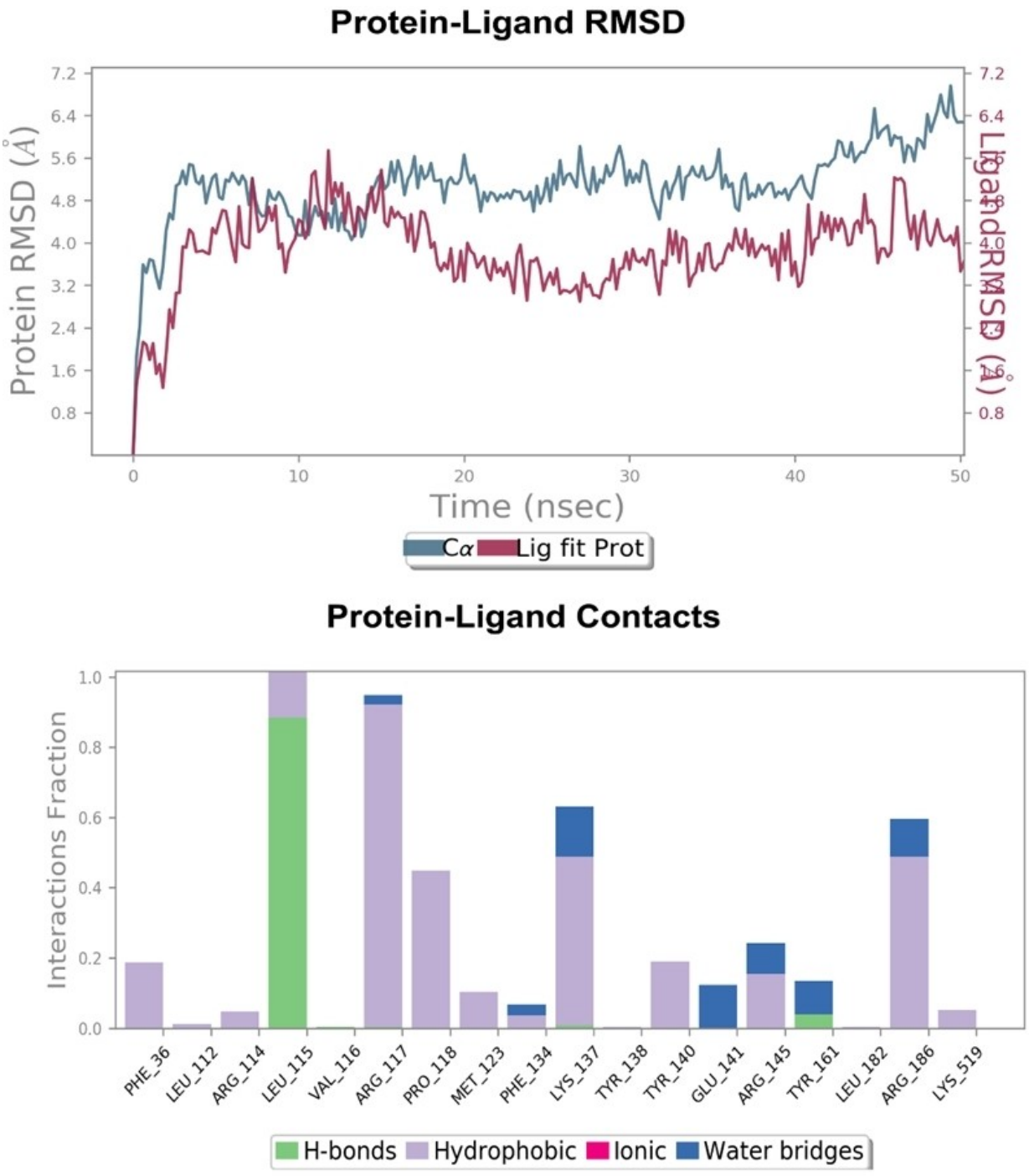

Figure 6. (a) RMSD plot of complex **ReL6** bound HSA in MD simulation (0–50 ns). **(b)** The histogram of the contact residues in complex **ReL6** bound HSA.

ism, $\Delta\varepsilon \sim 39\%$), coupled with a substantial intrinsic binding constant ($K_b = 0.44\times10^6\ M^{-1}$) and elevated apparent binding constant ($K_{app} = 2.28\times10^6\ M^{-1}$) signifies the good intercalation with ct-DNA.[32,48]

Assessment of Viscosity: This approach offers compelling evidence for elucidating the DNA binding mechanism of small molecules in solution. Intercalation induces a longitudinal expansion of DNA, enhancing its stiffness, and thereby elevating the viscosity in the solution. Conversely, partial intercalation or covalent binding results in a reduction in the effective DNA length, contributing to a slight decrease in the viscosity of the DNA solution. The relative viscosity of DNA remains unaffected when a drug interacts through groove binding or electrostatic interaction, as the binding process does not result in any change in the length of the DNA molecule. Metal complexes form connections with the external surface of DNA molecules through either Van der Waals forces or hydrophobic interactions in groove binding or electrostatic binding. The relative

viscosity of the DNA solution for complex **ReL6** was determined in comparison to Ethidium Bromide using an Ostwald viscometer following a standardized protocol.[32,49] The inclusion of complex **ReL6** in the ct-DNA solution leads to an increase in DNA viscosity, illustrating mainly the intercalative binding of the compound to ct-DNA with some degree of other interactions at varying concentration levels (Figure S14).

HSA Binding Study: Serum albumin (SA) is the major protein found in blood plasma, and interactions between drugs and proteins play a crucial role in drug transport, biodistribution, and potential toxicity. It is noteworthy that serum albumin contains a free thiol group from cysteine at position 34, and Re complexes demonstrate a remarkably high binding affinity for sulfur donors.[4,48] To assess the binding affinity of complex **ReL6** with HSA, fluorescence spectra of HSA was measured both in the absence and presence of metal complex. The excitation wavelength used was 280 nm, with emission recorded at 330 nm (Figure S15). The gradual decline in the emission intensity of HSA, correlating with an elevation in the concentration of the complex **ReL6**, indicates a substantial interaction between the metal complex and HSA. The Stern-Volmer quenching constant (K_{HSA}), binding affinity (K), the number of binding sites (n), and bimolecular quenching constant (K_q) for the complex **ReL6** was determined as $0.177\times10^6\ M^{-1}$, $1.49\times10^4\ M^{-1}$, 1.63, and $1.77\times10^{13}\ M^{-1}s^{-1}$ respectively, using the Stern-Volmer equation (v), equation (vi) and corresponding Stern-Volmer plots (Table 4). The determined K_q value for the complex **ReL6** exceeded the maximum conceivable value for dynamic quenching (2.0×10^{10} L.mol^{-1} s^{-1}), indicating the involvement of static quenching, effective bimolecular quenching, and bimolecular binding. In the Stern-Volmer plots, a concave-like upward curvature toward the Y-axis was noted at elevated quencher concentrations, signifying the establishment of a ground state complex between the complex and HSA.[32,33,49]

(Photo) generation of Singlet Oxygen: The efficiency of a photosensitizer (PS) in inducing the generation of singlet oxygen ($^1O_2$) species upon light excitation is crucial for the effectiveness of the photosensitizer in type II photodynamic therapy (PDT). Molecular oxygen ($^3O_2$) becomes excited through energy transfer from the excited T_1 state of PS, resulting in the generation of $^1O_2$. Singlet oxygen has an extremely short-term lifespan ($<$0.04-3 μs) and exhibits exceptionally high reactivity.[22,37] The efficiency of complex **ReL6** in generating singlet oxygen through photosensitization was determined using a UV spectrophotometer with 1,3-diphenylisobenzofuran (DPBF) and Rose Bengal (RB) following standard protocol.[50] In this study, under visible light irradiation (400-700 nm, 10 J.cm^{-2}), we observed a consistent decline in the absorbance of DPBF at 417 nm over time in the presence of complex **ReL6**. The plotted graph depicts the relative changes in DPBF absorbance at 417 nm (A/A_0) against the exposure time to visible light in seconds, where A symbolizes the DPBF absorbance at a specific time, while A_0 denotes the DPBF absorbance at t = 0 s. This analysis was conducted for both Rose Bengal and complex **ReL6** (Figure 7). The calculated singlet oxygen quantum yield for complex **ReL6** ($\phi_{\Delta ReL6}$) is 0.61, in comparison to the established singlet oxygen quantum yield of Rose Bengal ($\phi_{\Delta RB}=0.76$). Under similar experimental conditions, in the dark condition, there was no decline in DPBF absorbance at 417 nm (λ_{max}) with complex **ReL6**, suggesting that singlet oxygen generation did not occur under these circumstances. The high value of ϕ_Δ of complex **ReL6** confirmed that these types of complexes endured the PDT type II mechanism.

To further verify the generation of singlet oxygen, electron paramagnetic resonance (EPR) measurements were performed using 2,2,6,6-tetramethylpiperidine (TEMP) as spin trap agents.[51,52] As depicted in Figure S18a of the supporting information, a distinct $^1O_2$-induced triplet signal of TEMPO was observed following visible light irradiation for 60 min, indicating the $^1O_2$ formation, whereas no signal was detected in the absence of irradiation.

Photo-oxidation of NADH and Detection of H_2O_2, $O_2^{\bullet-}$, and $OH^\bullet$: The cytoplasm contains a substantial amount of the reduced form of nicotinamide adenine dinucleotide (NADH), a coenzyme. This plays a pivotal role in regulating energy production within mitochondria to a certain extent. An imbalance in the ratio of NADH to NAD^+ can lead to the suppression of the electron transport chain within the mitochondria, causing cellular dysfunction.[53,54] To assess the ability of the complex to initiate photocatalytic oxidation of the coenzyme in oxygenated solutions, complex **ReL6** at a concentration of 10 μM was placed in the presence of NADH (100 μM) within a solvent mixture comprising 20% MeOH and 80% H_2O (1:4, v/v). As shown in Figure S16, the UV-vis spectra of NADH showed no alterations when exposed to the complex in the absence of light. Nevertheless, under low concentrations, the absorbance of NADH gradually diminished after exposure to visible light irradiation (400-700 nm, 10 J.cm^{-2}) for the metal complex. Through assessing alterations at λ = 339 nm, the absorption peak of NADH, and turn over number (TON) were computed, revealing a remarkable value of 6.57 for 20 min light duration which favors Type I PDT pathway. Consequently, during photo-oxidation of NADH, complex **ReL6** procured electrons from NADH to form $NADH^{\bullet+}$. This radical species subsequently reacted with O_2, and producing H_2O_2. The presence of H_2O_2 was confirmed using peroxide test strips, which indicated its production (Figure S16c).[55] Furthermore, we assessed the ability of complex **ReL6** to generate $OH^\bullet$ radical using Methylene Blue (MB) as a probe.[56] Similar to the

Table 4. Binding parameters for the interaction of complex **ReL6** with HSA.

Complex	K_{HSA} [$\times10^6\ M^{-1}$][a]	k_q[$\times10^{13}\ M^{-1}s^{-1}$][b]	K [$\times10^4\ M^{-1}$][c]	N[d]
ReL6	0.177 ± 0.01	1.77 ± 0.20	1.49 ± 0.17	1.63 ± 0.08

[a] K_{HSA}, Stern-Volmer quenching constant. [b] K_q, quenching rate constant. [c] K, binding constant with HSA. [d] n, number of binding sites.

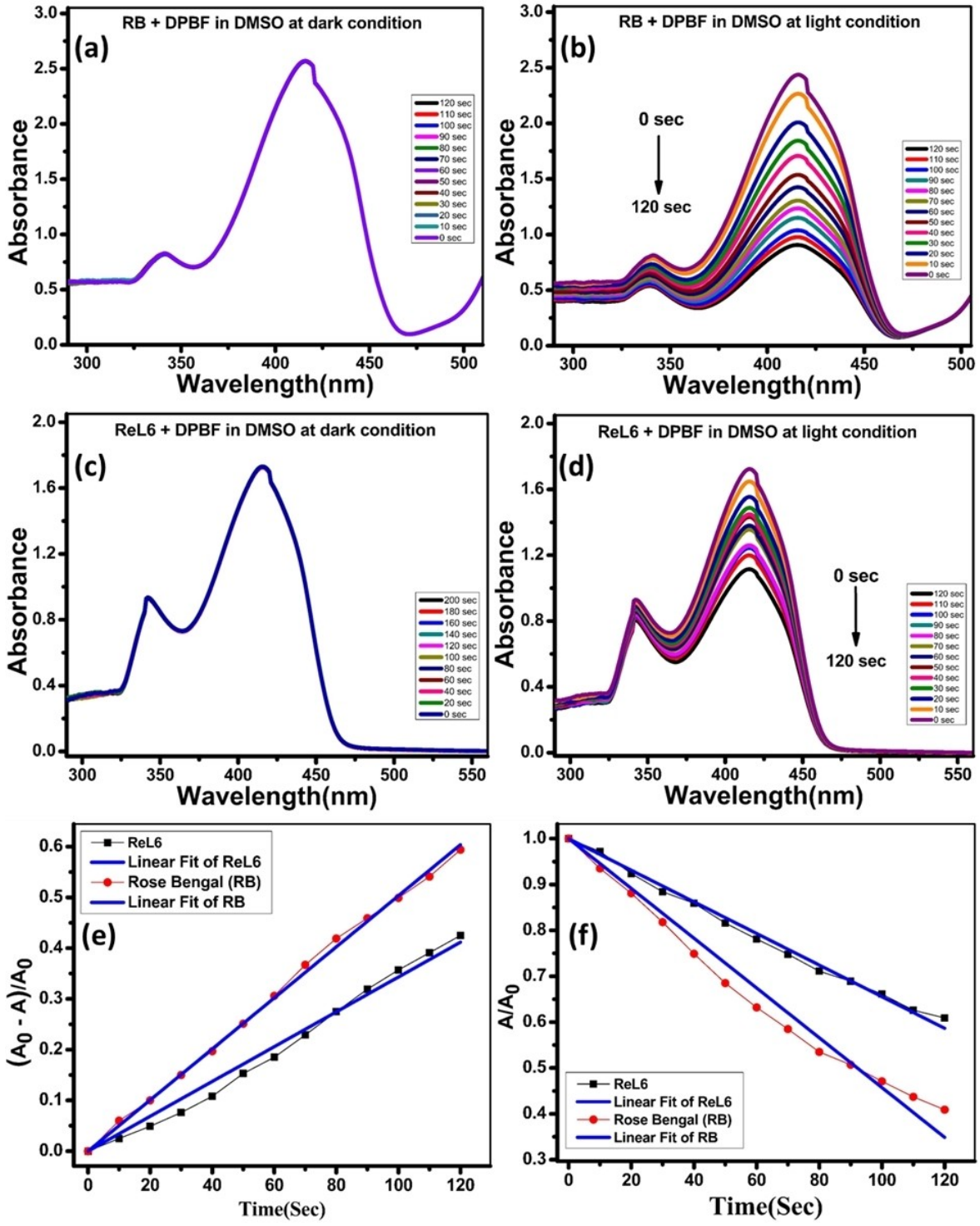

Figure 7. UV-visible spectroscopy investigations were conducted to examine the singlet oxygen generation in the presence of DPBF by Rose Bengal (RB) under dark conditions **(a)** and in the presence of light **(b)**, as well as by complex **ReL6** under dark conditions **(c)** and in the presence of light **(d)** at 298 K. A competitive plot depicting singlet oxygen generation between Rose Bengal and complex **ReL6**, expressed as $(A_0–A)/A_0$ versus time, was also generated **(e)**. Additionally, the relative change in absorbance by DPBF for Rose Bengal and complex **ReL6** at 417 nm (A/A_0) over time in seconds was analyzed **(f)**.

production of $^1O_2$, complex **ReL6** did not show significant $OH^•$ generation in the absence of light. However, there was a noticeable decrease in absorbance of MB after exposure to visible light, indicating the $OH^•$ generation (Figure S17). Additionally, the formation of $OH^•$ and $O_2^{•-}$ radicals by complex **ReL6** under visible light exposure was further confirmed using EPR spectroscopy. To achieve this, 5,5-dimethyl-1-pyrroline N-oxide (DMPO) was utilized as a probe or radical trapping agent.[52] A prominent six-line electron spin resonance signal originating from the DMPO/$O_2^{•-}$ adduct was seen in the spectra

under light irradiation (Figure S18b). Furthermore, in DMF-H_2O solution (2 : 98, v/v), a characteristic four-line resonance of the DMPO/$OH^{\bullet}$ adduct was identified in the spectra (Figure S18c). Hence, these results designated that complex **ReL6** is extremely effective photosensitizer for PDT against both normoxic and hypoxic tumors as it was accomplished for both Type I and Type II PDT pathways.

Intracellular ROS Generation by H_2DCFDA: Reactive oxygen species (ROS) are naturally generated as byproducts during various physiological processes within cellular metabolism. Elevated levels of ROS can lead to oxidative stress or inflammation, causing damage to cells and their components.[55] In photoactivated cancer therapy, controlled ROS production is utilized to selectively target and destroy cancer cells while preserving healthy ones. In photocatalytic cancer therapy, photoresponsive metal complexes have been found to generate hydrogen peroxide (H_2O_2), hydroxyl radicals ($OH^{\bullet}$), and superoxide anions ($O_2^{\bullet-}$) as byproducts of NADH oxidation, along with singlet oxygen ($^1O_2$) produced through a type II energy transfer pathway.[56] Here, in MDA-MB-231 breast cancer cells, the complex **ReL6** produced reactive oxygen species (ROS) under photo-irradiation indicating oxidative stress and subsequent cell death. The formation of green fluorescent 2′, 7′-dichlorofluorescein (DCF) by deacetylation and subsequent oxidation of nonfluorescent 2′, 7′-dichlorofluorescin diacetate (DCFDA) by cellular esterases and ROS designated the degree of ROS generation. The generation of ROS was less under dark condition which showed less intense cellular images at λ_{ems} 530 nm. However, upon light irradiation, significantly increase in fluorescence intensity was observed as higher rate of DCF formation, revealing the notable phototoxicity of complex **ReL6** (Figure 8).

Co-localization Study: In exploring the subcellular localization of complex **ReL6**, cells treated with complex **ReL6** were subjected to dual staining with Hoechst and Mitotracker Red. Subsequently, a thorough examination of their distribution within the cellular milieu was carried out using fluorescence microscopy and in which complex **ReL6** (10 μM) exhibited cytoplasmic localization. The subcellular positioning was observed through the green fluorescence emission of the complex with Hoechst and the red fluorescence emission with Mitotracker Red, providing insights into their respective distributions

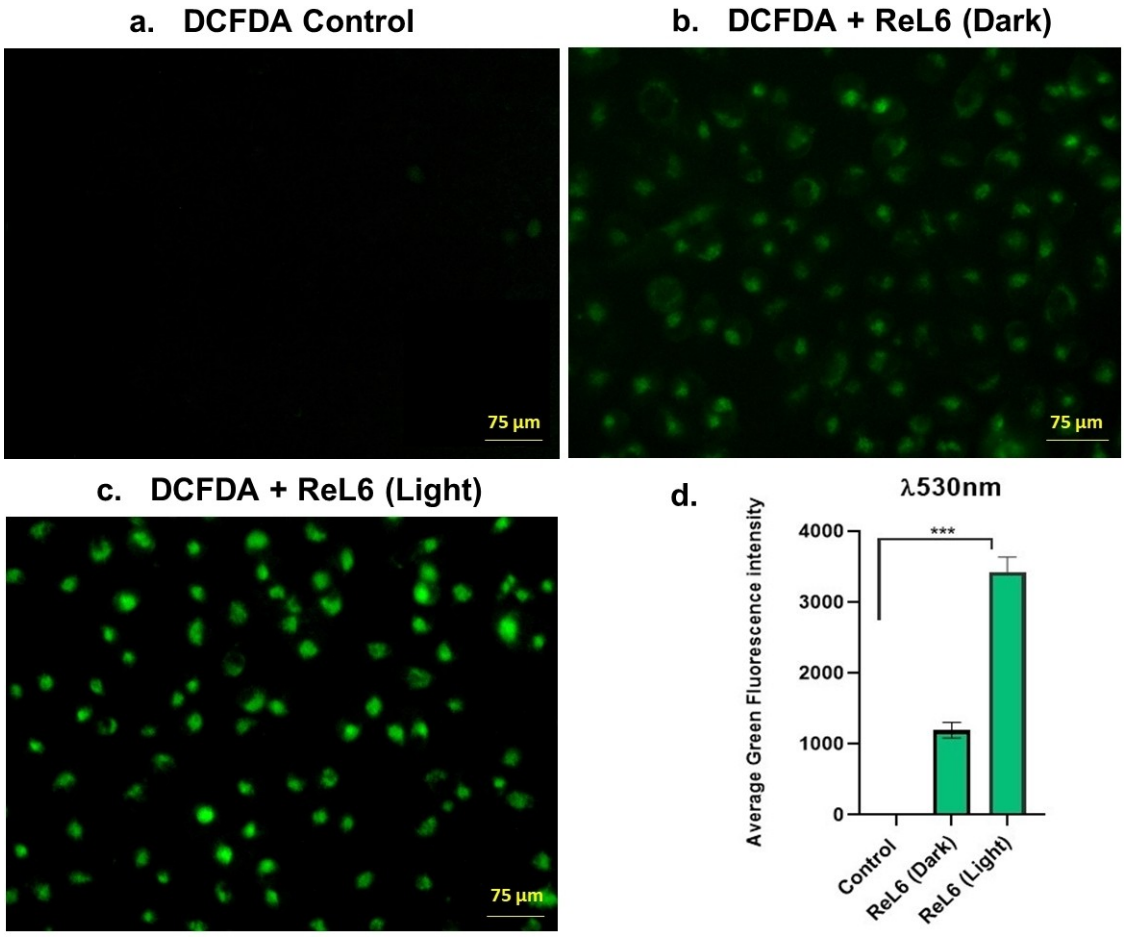

Figure 8. DCFDA assay for assessing the intracellular ROS production in MDA-MB-231 cells: (**a**) Untreated control cells (**b**) complex **ReL6** treatment of cells in dark condition (**c**) complex **ReL6** treatment of cells under visible light irradiation (400–700 nm, 10 $J.cm^{-2}$) for 1 h (incubation time of 4 h and concentration of 10 μM) (**d**) bar graph representing the average green fluorescence intensity of DCF under dark and light condition after **ReL6** treatment. Scale bar −75 μm. One-way ANOVA was utilised to get the p value between the groups. The observed p value was <0.0001 (***). The error bar represents the ± standard error of mean (SEM).

within the cellular context (Figure 9). The co-localization study using Mitotracker Red revealed the intracellular localization of complex **ReL6** within the mitochondria of MDA-MB-231 cells, as indicated by Pearson's coefficient of correlation (r = 0.918). Given the known impact of these complexes on cellular energetics and the mitochondria being a primary target, our focus shifted to assessing mitochondrial damage correlated with elevated reactive oxygen species (ROS) generation.

Photoinduced CO Release Property: Further exploration has been undertaken about the use of carbon monoxide (CO) as a cytotoxic agent for eliminating malignant cells. The probable mechanism involves the high-affinity binding of CO to cytochrome c oxidase, leading to the inhibition of the mitochondrial respiration pathway. By impeding mitochondrial respiration through CO binding, the proliferation of cancer cells is diminished, ultimately depleting cells metabolically.[30,56,57] In this work, initially, we performed the photoinduced CO Release study under visible light exposure (400-700 nm, 10 J.cm^{-2}). Unfortunately, no significant spectral changes were observed in the electronic spectrum of the complex **ReL6** under these conditions. Additionally, the myoglobin assay, conducted under reduced conditions, did not detect any photoinduced CO release when exposed to visible light. However, we observed notable changes when the complex **ReL6** was exposed to UV light ($\lambda = 305$ nm, 5 mW cm^{-}), which suggests that the complex may require higher energy light (shorter wavelengths) to trigger CO release.[56] The photoinduced CO release of complex **ReL6** was systematically performed by exposing the complex to higher-energy UV light irradiation ($\lambda = 305$ nm, 5 mW cm^{-2}) over a specified time duration. The ensuing alterations in the complex were meticulously examined through UV-Vis and IR spectroscopy in CH_3CN solution. After light exposure at several time intervals, there was a decrease in absorbance at 297 nm indicating the photoinduced CO release from the complex. The CO release rate ($K_{CO} = 0.44 \pm 003$ min^{-1}, conc. 100 μM) was calculated from the changes in absorbance with time (Figure S19). The K_{CO} value and a substantial decrease in the intensity of the CO stretching band at 2021 cm^{-1} upon 30 min of UV illumination in the IR study indicated the liberation of only one CO molecule which is trans to a σ-donating ligand Cl^{-} (Figure S20a).[13,58] The complex **ReL6** dissolved in acetonitrile was subjected to periodic exposure of UV light (305 nm). Subsequently, the photolyzed sample was dried, and IR spectra were obtained within KBr matrices.[13] The release of CO from complex **ReL6** was further confirmed by myoglobin assay.[13,53] In this standard assay, a noticeable alteration was observed in the soret band of reduced Mb, shifting from 432 nm to 421 nm (a blue shift of 11 nm) (Figure S20b). Additionally, new bands emerged at 540 and 577 nm. This spectral shift served as confirmation of the formation of the Mb–CO complex, affirming the release of CO induced by UV light (305 nm).

***In vitro* Phototoxicity of Re(I) Complexes**: The cell viability assays of the synthesized Re(I) complexes were investigated in triple-negative breast cancer cells (MDA MB-231) besides normal MRC-5 cells under dark and light exposure in the presence and absence of GSH in triplicates. The typical 3-(4,5-dimethylthiazol-2-yl)-2,5-diphenyltetrazolium bromide (MTT) assay protocol was implemented for the cytotoxicity assay with photofrin as a control PDT drug. The cells were incubated with the complexes along with photofrin and irradiated by yellow light (0-2 J.cm^{-2}) from a 400 W tungsten lamp fitted with a heat isolation filter and 500 nm long pass filter at an intensity of 4 mW/cm^2 for 4 h. The normalized cell viability *vs* log [complex] was plotted, and a nonlinear regression analysis was performed using Origin 8.5 to determine the IC_{50} values (Figure S21, Table 5). The light and dark toxicity of all these Re(I) complexes was reconnoitered in both normoxia and hypoxia environments. As shown in Table 5, all these complexes displayed insignificant dark toxicity against the TNBC cells (IC_{50}~61-79 μM). Interestingly, the dark toxicity was fond to be lower in hypoxic environment than normoxia might be due to strong complex-GSH adduct overcome the GSH-GSSG redox. However, a significant increase of toxicity (IC_{50}~6-29 μM) against TNBC was observed in yellow light irradiation under both normoxia

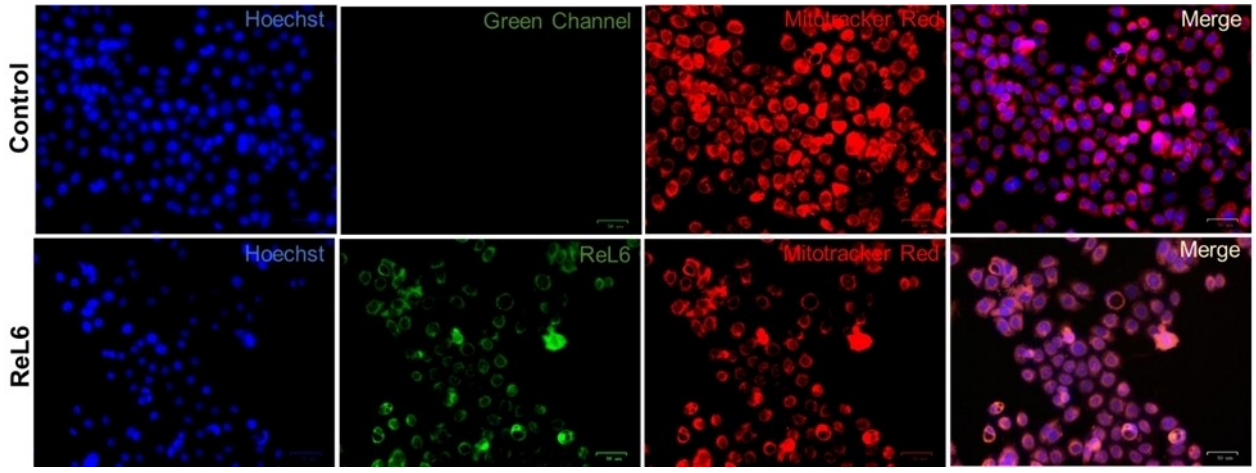

Figure 9. In the co-localization study, cytoplasmic localization of complex in MDA-MB-231 cells was observed. Co-staining with Mitotracker Red and Hoechst suggested potential mitochondrial localization. The calculated Pearson coefficient was 0.918 for complex **ReL6**. The scale bar in the image corresponds to 25 μm.

Table 5. Table for Phototoxicity of all the synthesized complexes (**ReL1**–**ReL6**).

Complex	IC_{50} (μM)[a]								
	MDA-MB-231[b]						MRC-5[c]		
	Normoxia[d]			Hypoxia[e]			Normoxia		
	Dark	In light[f]	PI[g]	Dark	In light	PI	Dark	In light	SF[h]
ReL1	62.55 ± 3.3	29.35 ± 4.1	2.13	79.91 ± 2.3	32.46 ± 3.6	2.46	99.02 ± 1.2	97.02 ± 1.1	3.30
ReL2	67.76 ± 5.3	25.27 ± 1.4	2.68	75.18 ± 0.5	28.81 ± 2.4	2.60	98.06 ± 0.7	96.81 ± 1.6	3.88
ReL3	69.54 ± 3.3	31.73 ± 4.3	2.19	72.19 ± 1.3	31.15 ± 1.3	2.31	> 100	> 100	> 3.15
ReL4	64.36 ± 2.6	23.08 ± 0.5	2.78	73.90 ± 3.1	21.15 ± 1.5	3.49	> 100	> 100	> 4.33
ReL5	65.61 ± 1.4	17.90 ± 0.5	3.66	75.08 ± 1.2	19.38 ± 1.7	3.87	96.06 ± 0.6	95.06 ± 1.6	5.31
ReL6	61.76 ± 1.2	6.24 ± 1.6	9.89	61.54 ± 2.1	6.40 ± 1.5	9.61	97.06 ± 1.3	94.06 ± 0.9	15.07
Photofrin	38.3 ± 0.5	3.02 ± 0.2	12.7	43.3 ± 0.56	6.92 ± 0.4	6.25	70.3 ± 1.2	65.22 ± 0.3	21.59

[a] 50% of cells experience cell death. [b] Triple negative human breast cancer cell line. [c] Normal Fibroblast. [d] 20–21% oxygen. [e] 2–6% oxygen. [f] Yellow light (0–2 J cm^{-2}) from a 400 W tungsten lamp fitted with a heat isolation filter and 500 nm long pass filter at an intensity of 4 m W/cm^2 for 4 h. [g] Phototoxicity Index. [h] Selectivity Factor. Based on the Student's t-test with Origin 8.5 software, statistical significance is denoted as $P < 0.05$. The error bar represents the ± standard error of mean (SEM).

and hypoxia environments. In sharp contrast, complex **ReL6** displayed the highest cytotoxic behavior (IC_{50}~6 μM, PI > 9) under yellow light irradiation compared to dark conditions. The order of light toxicity was observed as **ReL6** > **RrL5** > **ReL4** > **ReL2** > **ReL1** > **ReL3** which has been pointedly correlated with the lipophilicity and cellular uptake of these complexes. The drug transportation, cellular uptake, and DNA damaging ability of these complexes are the key factor in their antitumor potency evaluation. The significant potency of complex **ReL6** under photo irradiation can be ascribed to (i) potential binding with serum albumin for transportation, (ii) highest level of lipophilicity for cellular entry, (iii) strong complex-cysteine interaction and excessive production of ROS under normoxia and hypoxia environments (PDT type I and II) stop GSH biosynthesis and triggered GSH to GSSG conversion respectively, (iv) strong DNA intercalation, cellular DNA damage by singlet oxygen (PDT type II, normoxia) and several radicals (PDT Type I, hypoxia), (v) significant mitochondrial accumulation and mt-DNA damage by oxidative stress, (vi) Photoinduced CO release encumber mitochondrial respiration through CO binding and deplete cells metabolically. In contrast, photofrin exhibited good photo-selectivity in TNBC under normoxia but a loss in activity was observed against hypoxic tumors (Table 5). Therefore, complex **ReL6** is bringing forth a valuable drug in cancer therapy in the presence of light under hypoxic tumor ruling over the prevailing PDT drug, photofrin. The antitumor potency of the molecules also depends on their selectivity towards annihilating cancer cells over noncancerous cells. Herein, we observed that all these complexes are 3–15 folds more selective in TNBC cells compared to normal MRC-5 cells (Table 5).

3. Conclusions

In summary, we have synthesized and characterized novel Re(I) tricarbonyl complexes (**ReL1**-**ReL6**) to achieve GSH stable, hypoxia efficient, highly cytoselective anti-TNBC metal complexes. The presence of substituted imidazo[4,5-f][1,10]phenanthrolin-2-yl)phenol moiety imparted attractive photo-physical properties and increase the $^3\pi$-π^* character of T_1 state for effective PDT. The dark and light cytotoxicity of all these complexes was explored in both normoxia and hypoxia conditions. Notably, complex **ReL6** exhibited outstanding potency and selectivity (IC_{50}~6 μM, PI > 9) under yellow light irradiation compared to dark. The order of light toxicity was found to be **ReL6** > **RrL5** > **ReL4** > **ReL2** > **ReL1** > **ReL3** which has been pointedly correlated with the lipophilicity and cellular uptake (*via* ICP-MS) of these complexes. Interestingly, these complexes are 3-15 folds more selective in TNBC cells compared to normal MRC-5 cells. The role of most potent complex **ReL6** in type I and type II PDT was investigated by singlet oxygen ($^1O_2$) generation study using a DBPF probe, photooxidation of NADH to NAD^+ measurement, and Intracellular ROS generation study with H_2DCFDA. Photoinduced CO release of the complex **ReL6** was thoroughly performed by exposing the complex to higher-energy UV light irradiation (λ = 305 nm, 5 mW.cm^{-2}) over a specified time duration. The high value of fluorescence quantum yield ($\Phi_f = 0.50$) and substantial emission in the range of λ_{ems} 500-750 nm (visible to NIR range) of complex **ReL6** certainly helps in bio-imaging application as well. The extensively flat N^N chelating ligand also enhanced the DNA intercalation property of the complex. The labile chlorine and CO group improved the covalent interaction with DNA and facilitated interactions with other biomolecules such as human serum albumin (HSA), and glutathione (GSH). The strong lipophilic rhenium component and hydrophobic N^N chelating ligands increased the cellular uptake and localization in mitochondria which was measured by co-localization study using Mitotracker Red. The higher phototoxicity of complex **ReL6** is due to its high absorbance within the visible region, high $^1O_2$ quantum yield (type II PDT), and higher TON for NADH photo-oxidation (type I PDT). Although, this complex formed stable adduct with GSH under dark, it could not inhibit the light toxicity of the complex because the excess GSH in tumor cells

was depleted by strong complex-cysteine interaction, excessive ROS production under photo-irradiation. The transportation, cellular entry and mechanism of action of complex **ReL6** in the cell were triggered by the following steps: (i) strong complex-albumin adduct facilitates cellular transportation, (ii) cell penetration by high lipophilic character and accumulation in Mitochondria (PCC = 0.918) and expedites the Mitochondrial pathway, (iii) nuclear and mitochondrial DNA intercalation and damage by ROS under light irradiation, (iv) photo induced released CO bind with cytochrome c oxidase and inhibit the mitochondrial respiration. It's noteworthy to mention that Re(I) tricarbonyl complexes have not been well explored for photo-oxidation of NADH in aqua-rich conditions, and this study might open an opportunity to discover the efficacy of Re(I) tricarbonyl complexes to oxidize NADH more effectively for photocatalytic cancer therapy. Therefore, complex **ReL6** emerges as a promising option for cancer treatment using light therapy against hypoxic tumors, surpassing the current PDT drug, photofrin, which loses effectiveness in such conditions. Overall, complex **ReL6** represents a typical class of combined PDT and PACT agent that can generate $^1O_2$ as well as oxidize NADH and could also be developed as TNBC phototheranostic agent in near future.

Experimental Section

Materials and Method: We hired a variety of reagents and solvents, all with the highest commercial grade and purity, in all our tests. Every chemical and organic solvent used in chemical synthesis and chromatography was purchased from Sigma Aldrich, E-Merck (India), TCI Chemicals India, Sisco Research Laboratories Pvt. Ltd. (SRL) - India, and Spectrochem. A mixture of ethyl acetate and methanol was used as the solvent system for thin-layer chromatography using pre-coated silica gel 60 F254 aluminum sheets from E. Merck in Germany. Sigma Aldrich Chemical Limited provided ct-DNA, Human serum albumin (HSA), L-Glutathione reduced, N-Acetyl-L-cysteine, Ethidium bromide, and myoglobin. We bought all the cell lines from the National Centre for Cell Science (NCCS), Pune, India. Tetramethylsilane (TMS) served as the internal standard as the ^{1}H NMR and ^{13}C NMR spectra were collected on a 400 MHz Advanced Bruker DPX spectrometer. In ppm units, the chemical shifts (δ) were displayed. For example, s stands for singlet; brs for broad singlet; d for doublet; dd for double doublet; t for triplet; and m for multiplet. EPR spectra were recorded using an EMX Plus X-Band spectrometer (BRUKER BIOSPIN, Germany). Using an open capillary tube and an Elchem Microprocessor-based DT equipment, the melting points of the complexes were assessed. TDS conductometer-307 and Ostwald Viscometer were used to measure conductivity and viscosity respectively. A Shimadzu Affinity FT-IR spectrometer recorded IR spectra in the 4000-400 cm^{-1} range. On a Shimadzu ESI-MS-4000 mass spectroscopic apparatus with a 4000 triple quadrupole MS, the mass spectra of the synthesized compounds were computed. For elemental analysis, PerkinElmer equipment was used. Fluorescence spectra were taken using a Hitachi F7000 fluorescence spectrophotometer coupled with a xenon lamp, and UV-visible spectra were taken using a JASCO V-730 spectrophotometer utilizing a 1 cm quartz cell. Utilizing an Elisa reader and a 96-well plate, the cytotoxicity (MTT) assay was conducted.

Synthesis

General Synthetic Procedure of Ligands [L1–L6]

The ligands were synthesized based on our previously reported procedure.[32,33] The 1H-imidazo[4,5-f][1,10]phenanthrolin-2-yl)phenol ligands, denoted as **L1**-**L6**, were synthesized by reacting an equimolar combination of 1,10-phenanthroline-5,6-dione and different derivatives of benzaldehyde (**1**-**6**) in the presence of ammonium acetate in glacial acetic acid, as illustrated in Scheme 1.

2,4-dichloro-6-(1H-imidazo[4,5-f][1,10]phenanthrolin-2-yl)phenol (L1): Yield: 92%; Colour: Peach White; Mp: 230 °C; R_f (pure methanol): 0.65; IR (cm^{-1}): υ Ar O–H stretching (3504.74), N–H stretching (3327.40), Ar C–H stretching (3054.43), C=N stretching (1679.81), Ar C=C stretching (1472.23), C–N stretching (1348.01), C–Cl stretching (797.18), Ar C–H bending (731.80); ^{1}H NMR (DMSO-d_6, 400 MHz): δ 8.93 (s, 2H, H_1, H_{10}), 8.72 (d, 2H, H_3, H_8, J = 4.0 Hz), 8.07 (s, 1H, H_{15}), 7.72 (s, 2H, H_2, H_9), 7.41 (s, 1H, H_{17}); ^{13}C NMR (DMSO-d_6, 100 MHz): δ 152.89, 151.73, 148.35, 143.53, 136.61, 134.73, 131.14, 130.48, 130.19, 129.56, 126.78, 123.99, 122.03; ESI-MS (MeOH): observed m/z = 382.0147 $[M+H]^+$, 403.9970 $[M+Na]^+$, calcd m/z = 382.0202 $[M+H]^+$, 403.0129 $[M+Na]^+$.

2-(4-bromophenyl)-1H-imidazo[4,5-f][1,10]phenanthroline (L2): Yield: 96%; Colour: Peach Pink; Mp: 210 °C; R_f (pure methanol): 0.60; IR (cm^{-1}): υ N–H stretching (3391.96), Ar C–H stretching (3083.85), C=N stretching (1685.53), Ar C=C stretching (1455.07), C–N stretching (1371.71), Ar C–H bending (737.52), C–Br stretching (653.98); ^{1}H NMR (DMSO-d_6, 400 MHz): δ 8.99 (s, 2H, H_1, H_{10}), 8.92 (d, 2H, H_3, H_8, J = 7.6 Hz), 8.24 (d, 2H, H_{15}, H_{19}, J = 6.4 Hz), 7.79 (t, 2H, H_2, H_9, J = 3.6 Hz), 7.57 (d, 2H, H_{16}, H_{18}, J = 6.0 Hz); ^{13}C NMR (DMSO-d_6, 100 MHz): δ 149.58, 148.38, 143.68, 134.26, 132.58, 132.48, 131.65, 130.24, 128.93, 125.54, 123.85, 122.74, 121.77; ESI-MS (MeOH): observed m/z = 375.0258 $[M+H]^+$, 397.0068 $[M+Na]^+$, calcd m/z = 375.0245 $[M+H]^+$, 397.0065 $[M+Na]^+$.

2-bromo-6-(1H-imidazo[4,5-f][1,10]phenanthrolin-2-yl)-4-nitrophenol (L3): Yield: 90%; Colour: Chrome Yellow; Mp: 240 °C, R_f (pure methanol): 0.58; IR (cm^{-1}): υ Ar O–H stretching (3605.26), N–H stretching (3386.25), Ar C–H stretching (3083.86), C=N stretching (1590.74), Ar C=C stretching (1478.77), N=O stretching (1401.13), C–N stretching (1330.04), N–O stretching (1282.63), C–Br stretching (802.90), Ar C–H bending (737.52); ^{1}H NMR (DMSO-d_6, 400 MHz): δ 9.04 (s, 3H, H_1, H_{10}, H_{17}), 8.98 (d, 2H, H_3, H_8, J = 6.4 Hz), 8.37 (s, 1H, H_{15}), 7.89 (t, 2H, H_2, H_9, J = 4.0 Hz); ^{13}C NMR (DMSO-d_6, 100 MHz): δ 159.44, 158.29, 149.09, 146.44, 143.67, 139.60, 135.57, 132.21, 129.45, 129.24, 126.41, 121.65, 120.84, 119.79, 116.90, 114.01; ESI-MS (MeOH): observed m/z = 355.2791 $[M–Br]^+$, 389.2638 $[M–NO_2]^+$, 433.2906 $[M–H]^+$, calcd m/z = 355.3130 $[M–Br]^+$, 389.2120 $[M-NO_2]^+$, 433.9889 $[M–H]^+$.

2-(2-chloro-8-methylquinolin-3-yl)-1H-imidazo[4,5-f][1,10]phenanthroline (L4): Yield: 92%; Colour: Raw Sienna; Mp: 220 °C; R_f (pure methanol): 0.69; IR (cm^{-1}): υ N–H stretching (3351.64), Ar C–H stretching (3167), sp^3 –CH stretching (3036.45), C=N stretching (1644.68), Ar C=C stretching (1437.09), C–N stretching (1377.43), Ar C–H bending (737.52), C–Cl stretching (619.02); ^{1}H NMR (DMSO-d_6, 400 MHz): δ 9.05 (d, 4H, H_1, H_3, H_8, H_{10}, J = 3.2 Hz), 9.03 (s, 1H, H_1, H_{22}), 7.84 (dd, 3H, H_2, H_9, H_{19}, J = 8.0 Hz), 7.47 (d, 1H, H_{18}, J = 7.2 Hz), 7.22 (t, 1H, H_{20}, J = 7.6 Hz), 2.54 (s, 3H, Methyl protons); ^{13}C NMR (DMSO-d_6, 100 MHz): δ 161.49, 156.30, 150.96, 148.37, 147.75, 143.91, 139.65, 137.71, 133.63, 133.20, 127.61, 124.42, 123.75, 122.99, 120.46, 119.83, 17.85; ESI-MS (MeOH): observed m/z = 396.1038 $[M+H]^+$, calcd m/z = 396.1016 $[M+H]^+$.

2-([1,1′:4′,1″-terphenyl]-4-yl)-1H-imidazo[4,5-f][1,10]phenanthroline (L5): Yield: 92%; Colour: Cream Orange; Mp: 200 °C; R_f (pure methanol): 0.74; IR (cm^{-1}): υ N–H stretching (3356.82), Ar C–H stretching (3078.14), C=N stretching (1668.38), Ar C=C stretching (1478.77), C–N stretching (1395.41), Ar C–H bending (737.52); ^{1}H NMR (DMSO-d_6, 400 MHz): δ 9.04 (d, 2H, H_1, H_{10}, J= 2.8 Hz), 8.97 (d, 2H, H_3, H_8, J=7.6 Hz), 8.42 (d, 2H, H_{15}, H_{19}, J= 8.0 Hz), 7.99 (d, 2H, H_{27}, H_{31}, J=8.0 Hz), 7.91 (d, 2H, H_2, H_9, J= 8.0 Hz), 7.86-7.80 (m, 4H, H_{21}, H_{22}, H_{24}, H_{25}), 7.75 (d, 2H, H_{16}, H_{18}, J= 7.6 Hz), 7.49 (t, 2H, H_{28}, H_{30}, J=7.6 Hz), 7.39 (t, 1H, H_{29}, J=7.2 Hz); ^{13}C NMR (DMSO-d_6, 100 MHz): δ 157.67, 153.94, 151.54, 148.41, 143.56, 140.26, 137.93, 134.55, 130.45, 130.26, 129.58, 126.78, 124.01, 121.94; ESI-MS (MeOH): observed m/z=449.1767 $[M+H]^+$, 471.1588 $[M+Na]^+$, calcd m/z=449.1766 $[M+H]^+$, 471.1586 $[M+Na]^+$.

Synthesis of [1,1′:4′,1″-terphenyl]-4-carbaldehyde (5)

The compound **5** was synthesized by modifying our previously reported procedure.[46] In a round-bottomed flask, A mixture of 0.2 g of 4-bromobenzaldehyde (1.08 mmol), 4-biphenylboronic acid (1.30 mmol), tetrakis(triphenylphosphine)palladium(0) (0.05 mmol), and K_2CO_3 (5.40 mmol) was dissolved in 15 mL of toluene and kept for stirring at 110 °C for 4 h. After completion, the reaction mixture was allowed to cool down to room temperature and added with 100 mL of ethyl acetate. The combined organic layer was washed with water and saturated $NaHCO_3$ solution. Under reduced pressure, the mixed organic layer was concentrated after being dried with anhydrous Na_2SO_4 and purified by column chromatography on silica gel. Yield: 75%; Colour: Ivory White; Mp: 120 °C; R_f (1:4 Ethyl acetate - Hexane): 0.64; ^{1}H NMR ($CDCl_3$, 400 MHz): δ 10.07 (s, 1H, –CHO proton), 7.99 (d, 2H, H_2, H_6, J=8.4 Hz), 7.82 (d, 2H, H_3, H_5, J=8.0 Hz), 7.73 (s, 4H, H_8, H_9, H_{11}, H_{12}), 7.67 (d, 2H, H_{14}, H_{18}, J= 6.8 Hz), 7.48 (t, 2H, H_{15}, H_{17}, J=7.6 Hz), 7.39 (t, 1H, H_{16}, J=7.2 Hz); ^{13}C NMR ($CDCl_3$, 100 MHz): δ 191.98, 146.71, 141.40, 140.33, 138.52, 135.24, 130.37, 128.93, 127.77, 127.75, 127.69, 127.55, 127.10.

2-(4-(1-benzyl-1H-tetrazol-5-yl)phenyl)-1H-imidazo[4,5-f][1,10]phenanthroline (L6): Yield: 90%; Colour: Orange; Mp: 260 °C; R_f (pure methanol): 0.65; IR (cm^{-1}): υ N–H stretching (3394.77), Ar C–H stretching (3020.83), sp^3 –CH stretching (2857.23), C=N stretching (1560.45), Ar C=C stretching (1425.95), C–N stretching (1332.46), Ar C–H bending (721.17); ^{1}H NMR (DMSO-d_6, 400 MHz): δ 9.02 (d, 2H, H_1, H_{10}, J=2.8 Hz), 8.96 (d, 2H, H_3, H_8, J= 8.0 Hz), 8.48 (d, 2H, H_{15}, H_{19}, J=8.0 Hz), 8.24 (d, 2H, H_{16}, H_{18}, J= 8.4 Hz), 7.83 (dd, 2H, H_2, H_9, J=8.0 Hz), 7.45 – 7.39 (m, 5H, H_{23}, H_{24}, H_{25}, H_{26}, H_{27}), 6.04 (s, 2H, H_{21}); ^{13}C NMR (DMSO-d_6, 100 MHz): δ 164.52, 150.66, 148.20, 144.12, 134.58, 132.77, 130.19, 129.41, 129.12, 128.84, 127.72, 127.61, 127.38, 123.74, 122.25, 56.69; ESI-MS (MeOH): observed m/z=455.1733 $[M+H]^+$, 477.1542 $[M+Na]^+$, calcd m/z=455.1733 $[M+H]^+$, 477.1552 $[M+Na]^+$.

Synthesis of 4-(1H-tetrazol-5-yl) benzaldehyde (6′)

The method used to create tetrazole **6′** (as seen in Scheme 1) serves as an example. Initially, 0.3 g 4-formylbenzonitrile (2.29 mmol) was taken in a 100 mL pear-shaped round-bottom flask. Then 0.6 g sodium azide (9.23 mmol), 100 mg copper iodide (CuI) as a catalyst, and 30 mL dimethylformamide (DMF) were added to it. Subsequently, the reaction mixture was kept for stirring at 120 °C for 30 h. The progression of the reaction was analyzed using TLC (1:4 ethyl acetate: n-hexane). After completion of the reaction, the mixture was allowed to cool down to room temperature and was extracted with acidified water (acidified with 20% aq. HCl) and ethyl acetate. The combined organic layer was separated and washed with water and brine. To obtain the relevant reaction product, the organic layer was dried over Na_2SO_4, filtered, and then the solvent was removed under vacuum. The reaction product was then purified over a brief pad of SiO_2. Yield: 80%; Colour: Yellowish white; Mp: 104 °C; R_f (1:4 Ethyl acetate: n-Hexane): 0.41; ^{1}H NMR ($CDCl_3$, 400 MHz): δ 10.06 (s, 1H, –CHO proton), 8.34 (d, 2H, H_2, H_6, J=8.4 Hz), 8.07 (s, 1H, –NH proton), 8.01 (d, 2H, H_3, H_5, J=8.0 Hz); ^{13}C NMR ($CDCl_3$, 100 MHz): δ 191.55, 162.85, 156.97, 137.57, 130.27, 127.80.

Synthesis of 4-(1-benzyl-1H-tetrazol-5-yl) Benzaldehyde (6)

Firstly, in a 50 mL pear-shaped round-bottom flask, 0.2 g tetrazole **6′** (1.15 mmol), benzyl bromide (1.15 mmol), and K_2CO_3 (2.87 mmol) were combined in 10 mL of DMF and agitated at 0 °C until the conversion was finished. The progression of the reaction was analyzed using TLC (1:4 ethyl acetate: n-hexane). After completion of the reaction, the mixture was added with 100 mL of ethyl acetate and stirred vigorously. Then the combined organic layer was washed several times with water and brine. To obtain the relevant reaction product **6**, the organic layer was dried over Na_2SO_4, filtered, and then the solvent was dried under a vacuum. The crude product was then purified over a brief pad of SiO_2. Yield: 85%; Colour: White; Mp: 110 °C; R_f (1:4 Ethyl acetate: n-Hexane): 0.75; ^{1}H NMR ($CDCl_3$, 400 MHz): δ 10.06 (s, 1H, –CHO proton), 8.32 (d, 2H, H_2, H_6, J=8.4 Hz), 7.99 (d, 2H, H_3, H_5, J=8.4 Hz), 7.42 (t, 2H, H_{11}, H_{13}, J=9.6 Hz), 7.39 (d, 3H, H_{10}, H_{12}, H_{14}, J=7.2 Hz), 5.83 (s, 2H, H_8); ^{13}C NMR (DMSO-d_6, 100 MHz): δ 191.66, 164.38, 137.40, 133.06, 132.79, 130.20, 129.14, 129.11, 128.50, 127.43, 57.07.

General Procedure for the Synthesis of Rhenium (I) Metal Complexes (ReL1-ReL6)

The metal complexes were synthesized by modifying our previously reported procedure.[46] Initially, 40 mg (0.110 mmole, 1 equiv.) of pentacarbonylchlororhenium(I) and 1.1 equiv. of the previously produced ligand (**L1-L6**) were added to the reaction vessel containing 15 ml of toluene. Afterward, the entire mixture was subjected to reflux for 6 hours while being stirred constantly. The progress of the reaction was evaluated using TLC with 100% methanol as the solvent solution. Once the reaction was complete, the reaction mixture was allowed to cool, and the resulting solid was filtered out and washed with hexane several times. After purifying the product and recrystallizing it, the yellow-colored fine crystals were obtained with a yield of 85-95%. The synthesized complexes (**ReL1-ReL6**) were characterized using various spectroscopic techniques to confirm their structure.

[$(CO)_3Re^ICl(K^2$-N,N-2,4-dichloro-6-(1H-imidazo[4,5-f][1,10]phenanthrolin-2-yl)phenol)] (ReL1): Yield: 88%; Color: Chrome Yellow; Mp: 218 °C; R_f (pure methanol): 0.72; IR (cm^{-1}): υ Ar O–H stretching (3611.44), N–H stretching (3391.64), Ar C–H stretching (3058.61), C=O stretching (2024.39), C=O stretching (1922.58, 1891.62), C=N stretching (1615.65), Ar C=C stretching (1410.19), C–N stretching (1257.63), C–Cl stretching (814.41), Ar C–H bending (725.89); ^{1}H NMR (DMSO-d_6, 400 MHz): δ 9.39 (s, 2H, H_1, H_{10}), 9.12 (s, 2H, H_3, H_8), 8.12 (s, 2H, H_2, H_9), 7.99 (s, 1H, H_{15}), 7.37 (s, 1H, H_{17}); ^{13}C NMR (DMSO-d_6, 100 MHz): δ 198.35, 195.19, 190.61, 151.57, 144.19, 141.76, 133.17, 132.85, 131.70, 129.18, 126.87, 125.78, 124.61, 122.79; ESI-MS (MeCN): observed m/z=685.9802 $[M–H]^+$, 687.9813 $[M+H]^+$, calcd m/z=685.9325 $[M–H]^+$, 687.9110 $[M+H]^+$; Anal. Calcd for $C_{22}H_{10}Cl_3N_4O_4Re$: C, 38.47; H, 1.47; N, 8.16. Found: C, 38.41; H, 1.46; N, 8.19.

[$(CO)_3Re^ICl(K^2$-N,N-2-(4-bromophenyl)-1H-imidazo[4,5-f][1,10]phenanthroline] (ReL2): Yield: 86%; Color: Yellow; Mp: 220 °C; R_f (pure methanol): 0.68; IR (cm^{-1}): υ N–H stretching

(3439.12), Ar C–H stretching (3130.27), C=O stretching (2023.53), C=O stretching (1884.73), C=N stretching (1573.64), Ar C=C stretching (1453.89), C–N stretching (1366.09), Ar C–H bending (692.71), C–Br stretching (644.17); ^{1}H NMR (DMSO-d_6, 400 MHz): δ 9.38 (d, 2H, H_1, H_{10}, J = 3.6 Hz), 9.25 (d, 2H, H_3, H_8, J = 7.6 Hz), 8.25 (d, 2H, H_{15}, H_{19}, J = 7.6 Hz), 8.17 (d, 2H, H_2, H_9, J = 4.0 Hz), 7.88 (d, 2H, H_{16}, H_{18}, J = 6.4 Hz); ^{13}C NMR (DMSO-d_6, 100 MHz): δ 198.19, 195.76, 190.63, 152.18, 151.58, 144.19, 137.64, 133.12, 132.95, 132.44, 131.67, 129.15, 126.81, 125.70, 122.77; ESI-MS (MeCN): observed m/z = 680.9338 $[M+H]^+$, 685.9855 $[(M–Cl)(CH_3CN)]^+$, 702.9177 $[M+Na]^+$, calcd m/z = 680.9160 $[M+H]^+$, 685.9838 $[(M–Cl)(CH_3CN)]^+$, 702.9158 $[M+Na]^+$; Anal. Calcd for $C_{22}H_{11}BrClN_4O_3Re$: C, 38.81; H, 1.63; N, 8.23. Found: C, 38.78; H, 1.61; N, 8.17.

$[(CO)_3Re^ICl(K^2$-N,N-2-bromo-6-(1H-imidazo[4,5-f][1,10]phenanthrolin-2-yl)-4-nitrophenol] (ReL3): Yield: 90%; Color: Dark Yellow; Mp: 258 °C; R_f (pure methanol): 0.66; IR (cm^{-1}): υ Ar O–H stretching (3579.11), N–H stretching (3351.23), Ar C–H stretching (3150.03), C=O stretching (2017.24), C=O stretching (1894.48), C=N stretching (1593.41), Ar C=C stretching (1430.79), N=O stretching (1401.23), C–N stretching (1363.14), N–O stretching (1179.48), Ar C–H bending (722.98), C–Br stretching (691.87); ^{1}H NMR (DMSO-d_6, 400 MHz): δ 9.39 (s, 1H, H_{17}), 9.26 (s, 1H, -OH proton), 9.09 (d, 2H, H_1, H_{10}, J = 21.2 Hz), 8.14 (s, 1H, -NH proton), 7.24 (d, 2H, H_2, H_9, J = 6.8 Hz), 7.18 (d, 3H, H_3, H_8, H_{15}, J = 7.6 Hz); ^{13}C NMR (DMSO-d_6, 100 MHz): δ 197.41, 194.66, 190.54, 157.81, 152.63, 148.04, 143.89, 136.85, 135.08, 131.12, 130.15, 126.52, 123.69; 121.94, 119.40, 117.47; ESI-MS (MeCN): observed m/z = 741.7419 $[M+H]^+$, calcd m/z = 741.7139 $[M+H]^+$; Anal. Calcd for $C_{22}H_{10}BrClN_5O_6Re$: C, 35.62; H, 1.36; N, 9.44. Found: C, 35.58; H, 1.29; N, 9.38.

$[(CO)_3Re^ICl(K^2$-N,N-2-(2-chloro-8-methylquinolin-3-yl)-1H-imidazo[4,5-f][1,10]phenanthroline] (ReL4): Yield: 85%; Color: Yellow Ochre; Mp: 240 °C; R_f (pure methanol): 0.76; IR (cm^{-1}): υ N–H stretching (3306.92), Ar C–H stretching (3178.78), sp3 –CH stretching (3044.19), C=O stretching (2027.96), C=O stretching (1922.38, 1875.64), C=N stretching (1641.93), Ar C=C stretching (1443.68), C–N stretching (1361.47), C–Cl stretching (899.69), Ar C–H bending (730.45); ^{1}H NMR (DMSO-d_6, 400 MHz): δ 11.50 (s, 1H, -NH proton), 9.36 (d, 1H, H_1, J = 4.4 Hz), 9.12 (d, 1H, H_{22}, J = 4.4 Hz), 8.98 (d, 1H, H_{20}, J = 12.0 Hz), 8.11 (d, 2H, H_3, H_8, J = 8.0 Hz), 7.73 (d, 1H, H_{18}, J = 7.2 Hz), 7.43 (d, 1H, H_{10}, J = 7.2 Hz), 7.35 (d, 1H, H_{19}, J = 7.2 Hz), 7.15 (t, 1H, H_2, J = 7.6 Hz), 7.08 (t, 1H, H_9, J = 7.6 Hz), 2.40 (s, 3H, Methyl protons); ^{13}C NMR (DMSO-d_6, 100 MHz): δ 197.75, 196.91, 190.75, 161.23, 150.82, 146.37, 140.47, 137.68, 133.54, 129.34, 127.70, 125.68, 124.24, 122.99, 119.52, 17.82; ESI-MS (MeCN): observed m/z = 706.0426 $[(M–Cl)(CH_3CN)]^+$, 722.0082 $[M+Na]^+$, 689.1051 $[(M–CO)(OH)]^+$, calcd m/z = 706.0530 $[(M–Cl)(CH_3CN)]^+$, 722.9851 $[M+Na]^+$, 689.0031 $[(M–CO)(OH)]^+$; Anal. Calcd for $C_{26}H_{14}Cl_2N_5O_3Re$: C, 44.51; H, 2.01; N, 9.98. Found: C, 44.46; H, 1.96; N, 9.92.

$[(CO)_3Re^ICl(K^2$-N,N-2-([1,1′:4′,1″-terphenyl]-4-yl)-1H-imidazo[4,5-f][1,10]phenanthroline] (ReL5): Yield: 90%; Color: Sandal Yellow; Mp: 224 °C; R_f (pure methanol): 0.78; IR (cm^{-1}): υ N–H stretching (3367.47), Ar C–H stretching (3152.51), C=O stretching (2019.55), C=O stretching (1885.09), C=N stretching (1591.30), Ar C=C stretching (1436.65), C–N stretching (1358.67), Ar C–H bending (722.11); ^{1}H NMR (DMSO-d_6, 400 MHz): δ 14.34 (s, 1H, -NH proton), 9.38 (d, 2H, H_1, H_{10}, J = 4.0 Hz), 9.27 (d, 2H, H_3, H_8, J = 8.0 Hz), 8.41 (d, 2H, H_{15}, H_{19}, J = 8.4 Hz), 8.15 (t, 2H, H_{27}, H_{31}, J = 7.6 Hz), 8.05 (d, 2H, H_2, H_9, J = 8.4 Hz), 7.94 (d, 2H, H_{16}, H_{18}, J = 8.4 Hz), 7.84 (d, 2H, H_{21}, H_{25}, J = 8.4 Hz), 7.76 (d, 2H, H_{22}, H_{24}, J = 7.6 Hz), 7.50 (t, 2H, H_{28}, H_{30}, J = 7.6 Hz), 7.39 (t, 1H, H_{29}, J = 7.6 Hz); ^{13}C NMR (DMSO-d_6, 100 MHz): δ 198.26, 196.95, 190.54, 155.96, 152.97, 151.80, 144.27, 134.0, 133.42, 131.09, 130.77, 128.90, 128.78, 127.83, 127.11, 126.97, 126.41, 125.71, 123.17; ESI-MS (MeCN): observed m/z = 755.4911 $[M+H]^+$, calcd m/z = 755.4240 $[M+H]^+$; Anal. Calcd for $C_{34}H_{20}ClN_4O_3Re$: C, 54.15; H, 2.67; N, 7.43. Found: C, 54.08; H, 2.60; N, 7.40.

$[(CO)_3Re^ICl(K^2$-N,N-2-(4-(1-benzyl-1H-tetrazol-5-yl)phenyl)-1H-imidazo[4,5-f][1,10]phenanthroline] (ReL6): Yield: 92%; Color: Lemon Yellow; Mp: 278 °C; R_f (pure methanol): 0.70; IR (cm^{-1}): υ N–H stretching (3330.29), Ar C–H stretching (3184.43), sp3 –CH stretching (3026.47), C=O stretching (2021.57), C=O stretching (1899.01), C=N stretching (1607.27), Ar C=C stretching (1437.23), C–N stretching (1367.12), Ar C–H bending (724.81); ^{1}H NMR (DMSO-d_6, 400 MHz): δ 14.47 (s, 1H, -NH proton), 9.38 (d, 2H, H_1, H_{10}, J = 4.8 Hz), 9.27 (d, 2H, H_3, H_8, J = 7.6 Hz), 8.48 (d, 2H, H_{15}, H_{19}, J = 8.4 Hz), 8.33 (d, 2H, H_{16}, H_{18}, J = 8.0 Hz), 8.15 (s, 2H, H_2, H_9), 7.46–7.39 (m, 5H, H_{23}, H_{24}, H_{25}, H_{26}, H_{27}), 6.06 (s, 2H, H_{21}); ^{13}C NMR (DMSO-d_6, 100 MHz): δ 198.29, 195.62, 190.62, 164.37, 152.18, 151.94, 144.38, 134.54, 133.36, 131.61, 129.43, 129.16, 128.88, 128.67, 128.57, 127.75, 127.63, 127.09, 125.78, 56.76; ESI-MS (MeCN): observed m/z = 766.1305 $[(M–Cl)(CH_3CN)]^+$, calcd m/z = 766.1325 $[(M–Cl)(CH_3CN)]^+$; Anal. Calcd for $C_{30}H_{18}ClN_8O_3Re$: C, 49.72; H, 2.50; N, 15.46. Found: C, 49.68; H, 2.59; N, 15.42.

Biology

Cell Culture

The cells were cultured in DMEM media (Gibco) with 10% fetal bovine serum (Himedia, India), 1% penicillin and streptomycin, and 1% Glutmax (Gibco, Thermo Scientific, USA) at 37 °C in 5% CO_2. The cells were trypsinized with 0.25 percent trypsin-EDTA when they achieved 70%–80% confluency (Thermo Fisher Scientific, USA).

In Vitro *Cytotoxic Study*

The *in vitro* cytotoxicity of complexes (**ReL1**-**ReL6**) was investigated by standard MTT assay protocol. The complexes were first dissolved in 0.1% DMSO, and then diluted in DMEM medium. The triple negative breast cancer cell line, MDA-MB-231, as well as one normal fibroblast (MRC-5) were used for the investigation. In 96-well plates, approximately 1×10^4 cells per well were cultivated in 100 μL of growth media and then incubated at 37 °C in a 5% CO_2 environment. The cells were subjected to a variety of concentrations, commencing with an initial concentration of 200 μM, and subsequently, a serial dilution was performed for all the complexes. This treatment was carried out in a 0.1% DMSO-containing media for duration of 4 h, all while being conducted in a light-restricted environment. In one set of cells, was maintained in darkness with the fresh DMEM medium for an additional 44 h; thus, cell cultures were incubated for 5 h at 37 °C with 100 μL of MTT reagent (1 mg/mL). The cells in the control wells also consumed the same volume of DMSO-DMEM. In another set of cells, following the exclusion of the compound-containing medium, 150 μL of DPBS was added to each well for light irradiation. Subsequently, the cells were exposed under yellow light (0–2 J.cm^{-2}) from a 400 W tungsten lamp fitted with heat isolation filter and 500 nm long pass filter at an intensity of 4 mW/cm^2 for 4 hours, and the cells were incubated in a CO_2 incubator for 40 hours. After that, the suspension from both the sets was placed on a micro vibrator for 10 minutes, and the absorbance was measured in an ELISA plate reader at 570 nm. Similar protocol has been followed in hypoxic environment. The experiment was likewise carried out three times. Photofrin was used as a standard positive control in this experiment. The data were reported as a percentage of growth inhibition, i.e. % growth inhibition = 100 [(AD×100)/AB], where AD represents measured absorbance in sample wells and AB represents measured absorbance in blank wells (cells with a medium and a vehicle).

Statistical Analysis

All experiments were conducted in triplicate, and appropriate statistical tests were used for comparisons. One-way ANOVA was utilised to compare the various groups, and multiple comparison tests were employed to get the p value between the groups. The observed p values are < 0.0001(***), < 0.001(**), < 0.01(*), < 0.05(ns: non-significant). The statistical p value in MTT assay was calculated based on Student's t-test using Origin 8.5 software. Error bars indicate the $\pm$ standard error of the mean (SEM).

4. Supporting Information Summary

NMR, FT-IR, and ESI-HRMS spectra of all compounds associated with this article as well as experimental procedures, plots and data related to biological studies, can be found in the accompanying supporting information available. The authors have cited additional references within the Supporting Information.[59–91]

Author Contributions

PP designed and supervised the project. BK conducted synthesis, characterization, biomolecular binding and cellular experiments, and data interpretation. Both the authors participated in the preparation and editing of the manuscript and approved its submission.

Acknowledgements

The authors are grateful to the Department of Science and Technology, Government of India for supporting the work through the DST-SERB CRG project grant (CRG/2021/002267). VIT University provided VIT SEED funding and DST; New Delhi provided DST-FIST project. The authors are thankful to them also.

Conflict of Interests

"There are no conflicts to declare".

Data Availability Statement

The data that support the findings of this study are available in the supplementary material of this article.

Keywords: Photodynamic therapy · Anticancer activity · 1H-imidazo[4,5-f][1,10]phenanthroline · Re(I) tricarbonyl complex · Medicinal inorganic chemistry

[1] W. Liu, R. Gust, *Chem. Soc. Rev.* **2013**, *42*, 755–773.
[2] K. D. Mjos, C. Orvig, *Chem. Rev.* **2014**, *114*, 4540–4563.
[3] W. Ma, L. Guo, Z. Tian, S. Zhang, X. He, J. Li, Y. Yang, Z. Liu, *Dalt. Trans.* **2019**, *48*, 4788–4793.
[4] J. Li, L. Guo, Z. Tian, S. Zhang, Z. Xu, Y. Han, R. Li, Y. Li, Z. Liu, *Inorg. Chem.* **2018**, *57*, 13552–13563.
[5] R. Ramos, J. F. Gilles, R. Morichon, C. Przybylski, B. Caron, C. Botuha, A. Karaiskou, M. Salmain, J. Sobczak-Thépot, *J. Med. Chem.* **2021**, *64*, 16675–16686.
[6] B. Kar, N. Roy, S. Pete, P. Moharana, P. Paira, *Inorg. Chim. Acta* **2020**, *512*, 119858.
[7] G. Gasser, N. Metzler-Nolte, *Curr. Opin. Chem. Biol.* **2012**, *16*, 84–91.
[8] G. Gasser, I. Ott, N. Metzler-Nolte, *J. Med. Chem.* **2011**, *54*, 3–25.
[9] U. Das, B. Kar, S. Pete, P. Paira, *Dalt. Trans.* **2021**, *50*, 11259–11290.
[10] S. Pete, N. Roy, B. Kar, P. Paira, *Coord. Chem. Rev.* **2022**, *460*, 214462.
[11] S. P. Vaidya, M. Manikandan, S. Chhatar, S. Dey, C. Patra, M. Patra, *Inorg. Chem. Front.* **2023**, *10*, 6711–6727.
[12] R. R. Ye, C. P. Tan, Y. N. Lin, L. N. Ji, Z. W. Mao, *Chem. Commun.* **2015**, *51*, 8353–8356.
[13] I. Chakraborty, S. J. Carrington, G. Roseman, P. K. Mascharak, *Inorg. Chem.* **2017**, *56*, 1534–1545.
[14] P. C. Kunz, W. Huber, A. Rojas, U. Schatzschneider, B. Spingler, *Eur. J. Inorg. Chem.* **2009**, *4*, 5358–5366.
[15] S. Clède, C. Policar, *Chem. Eur. J.* **2015**, *21*, 942–958.
[16] V. Schirrmacher, *Int. J. Oncol.* **2019**, *54*, 407–419.
[17] A. F. dos Santos, D. R. Q. de Almeida, L. F. Terra, M. S. Baptista, L. Labriola, *J. Cancer Metastasis Treat.* **2019**, *5*. DOI: 10.20517/2394-4722.2018.83.
[18] K. Muniyandi, B. George, T. Parimelazhagan, H. Abrahamse, *Molecules* **2020**, *25*. DOI: 10.3390/molecules25184102.
[19] X. D. Song, B. B. Chen, S. F. He, N. L. Pan, J. X. Liao, J. X. Chen, G. H. Wang, J. Sun, *Eur. J. Med. Chem.* **2019**, *179*, 26–37.
[20] G. Shi, S. Monro, R. Hennigar, J. Colpitts, J. Fong, K. Kasimova, H. Yin, R. DeCoste, C. Spencer, L. Chamberlain, A. Mandel, L. Lilge, S. A. McFarland, *Coord. Chem. Rev.* **2015**, *282–283*, 127–138.
[21] B. Kar, U. Das, N. Roy, P. Paira, *Coord. Chem. Rev.* **2023**, *474*, 214860.
[22] G. Gunaydin, M. E. Gedik, S. Ayan, *Front. Chem.* **2021**, *9*, 1–26.
[23] S. Monro, K. L. Colón, H. Yin, J. Roque, P. Konda, S. Gujar, R. P. Thummel, L. Lilge, C. G. Cameron, S. A. McFarland, *Chem. Rev.* **2019**, *119*, 797–828.
[24] H. S. Liew, C. W. Mai, M. Zulkefeli, T. Madheswaran, L. V. Kiew, N. Delsuc, M. Lee Low, *Molecules* **2020**, *25*, 1–23.
[25] A. Leonidova, G. Gasser, *ACS Chem. Biol.* **2014**, *9*, 2180–2193.
[26] J. O. Yoo, K. S. Ha, *New Insights into the Mechanisms for Photodynamic Therapy-Induced Cancer Cell Death*, International Review of Cell and Molecular Biology, 295, **2012**, 139–174. Elsevier Inc. **2012**.
[27] D. A. Kurtz, K. R. Brereton, K. P. Ruoff, H. M. Tang, G. A. N. Felton, A. J. M. Miller, J. L. Dempsey, *Inorg. Chem.* **2018**, *57*, 5389–5399.
[28] D. Álvarez, M. I. Menéndez, R. López, *Inorg. Chem.* **2022**, *61*, 439–455.
[29] A. E. Pierri, A. Pallaoro, G. Wu, P. C. Ford, *J. Am. Chem. Soc.* **2012**, *134*, 18197–18200.
[30] S. C. Marker, S. N. MacMillan, W. R. Zipfel, Z. Li, P. C. Ford, J. J. Wilson, *Inorg. Chem.* **2018**, *57*, 1311–1331.
[31] M. Annereau, F. Martial, J. Forté, G. Gontard, S. Blanchard, H. Dossmann, M. Salmain, V. Corcé, *Appl. Organomet. Chem.* **2023**, *37*, 1–12.
[32] B. Kar, U. Das, S. De, S. Pete, A. Sharma S, N. Roy, A. K. Ashok, D. Panda, P. Paira, *Dalt. Trans.* **2021**, *50*, 10369–10373.
[33] B. Kar, S. Shanavas, A. H. Nagendra, U. Das, N. Roy, S. Pete, A. Sharma S, S. De, A. Kumar S K, S. Vardhan, S. K. Sahoo, D. Panda, S. Shenoy, B. Bose, P. Paira, *Dalt. Trans.* **2022**, *51*, 5494–5514.
[34] J. Yang, J. X. Zhao, Q. Cao, L. Hao, D. Zhou, Z. Gan, L. N. Ji, Z. W. Mao, *ACS Appl. Mater. Interfaces* **2017**, *9*, 13900–13912.
[35] A. J. Amoroso, R. J. Arthur, M. P. Coogan, J. B. Court, V. Fernández-Moreira, A. J. Hayes, D. Lloyd, C. Millet, S. J. A. Pope, *New J. Chem.* **2008**, *32*, 1097–1102.
[36] F. Wang, J. Liang, H. Zhang, Z. Wang, Q. Wan, C. Tan, L. Ji, *ACS Appl. Mater. Interfaces* **2019**, *11*, 13123–13133.
[37] T. M. Kirse, I. Maisuls, M. P. Denofrio, A. Hepp, F. M. Cabrerizo, C. A. Strassert, *Organometallics* **2024**, *43*(16), 1752–1765.
[38] R. R. Ye, C. P. Tan, M. H. Chen, L. Hao, L. N. Ji, Z. W. Mao, *Chem. A Eur. J.* **2016**, *22*, 7800–7809.
[39] V. Pierroz, T. Joshi, A. Leonidova, C. Mari, J. Schur, I. Ott, L. Spiccia, S. Ferrari, G. Gasser, *J. Am. Chem. Soc.* **2012**, *134*, 20376–20387.
[40] E. B. Bauer, A. A. Haase, R. M. Reich, D. C. Crans, F. E. Kühn, *Coord. Chem. Rev.* **2019**, *393*, 79–117.
[41] S. Banerjee, I. Pant, I. Khan, P. Prasad, A. Hussain, P. Kondaiah, A. R. Chakravarty, *Dalt. Trans.* **2015**, *44*, 4108–4122.

[42] M. Saldías, N. Guzmán, F. Palominos, C. Sandoval-Altamirano, G. Günther, N. Pizarro, A. Vegá, *ACS Omega* **2019**, *4*, 4679–4690.
[43] T. Auvray, B. D. Secco, A. Dubreuil, N. Zaccheroni, G. S. Hanan, *Inorg. Chem.* **2021**, *60*, 70–79.
[44] C. McBeth, *ChemElectroChem* **2023**, *10*, e2023001.
[45] R. Ruswanto, T. Nofianti, R. Mardianingrum, D. Kesuma, Siswandono, *Heliyon* **2022**, *8*. DOI: 10.1016/j.heliyon.2022.e10694.
[46] R. Das, P. Paira, *Dalt. Trans.* **2023**, *52*, 15365–15376.
[47] L. T. Babu, P. Paira, *New J. Chem.* **2021**, *45*, 20447–20458.
[48] L. E. Enslin, K. Purkait, M. D. Pozza, B. Saubamea, P. Mesdom, H. G. Visser, G. Gasser, M. Schutte-Smith, *Inorg. Chem.* **2023**, *62*, 12237–12251.
[49] U. Das, S. Shanavas, A. H. Nagendra, B. Kar, N. Roy, S. Vardhan, S. K. Sahoo, D. Panda, B. Bose, P. Paira, *ACS Appl. Bio Mater.* **2023**, *6*, 410–424.
[50] M. Pal, V. Ramu, D. Musib, A. Kunwar, A. Biswas, M. Roy, *Inorg. Chem.* **2021**, *60*, 6283–6297.
[51] F. Fan, L. Wang, F. Li, Y. Fu, H. Xu, *ACS Appl. Mater. Interfaces* **2016**, *8*, 17004–17010.
[52] Q. Ren, H. Wang, D. Li, A. Dao, J. Luo, D. Wang, P. Zhang, H. Huang, *Adv. Healthcare Mater.* **2024**, p. 2304067.
[53] J. Kasparkova, A. Hernández-García, H. Kostrhunova, M. Goicuría, V. Novohradsky, D. Bautista, L. Markova, M. D. Santana, V. Brabec, J. Ruiz, *J. Med. Chem.* **2024**, *67*(1), 691–708.
[54] M. Tian, J. Li, S. Zhang, L. Guo, X. He, D. Kong, H. Zhang, Z. Liu, *Chem. Commun.* **2017**, *53*, 12810–12813.
[55] R. Kushwaha, A. Upadhyay, S. Peters, A. K. Yadav, A. Mishra, A. Bera, T. Sadhukhan, S. Banerjee, *Langmuir* **2024**, *40*, 12226–12238.
[56] R. Kushwaha, V. Singh, S. Peters, A. K. Yadav, T. Sadhukhan, B. Koch, S. Banerjee, *J. Med. Chem.* **2024**, *67*, 6537–6548.
[57] S. J. Carrington, I. Chakraborty, J. M. L. Bernard, P. K. Mascharak, *Inorg. Chem.* **2016**, *55*, 7852–7858.
[58] S. Sato, Y. Matubara, K. Koike, M. Falkenström, T. Katayama, Y. Ishibashi, H. Miyasaka, S. Taniguchi, H. Chosrowjan, N. Mataga, N. Fukazawa, S. Koshihara, K. Onda, O. Ishitani, *Chem. A Eur. J.* **2012**, *18*, 15722–15734.
[59] C. Liu, L. Zhou, F. Wei, L. Li, S. Zhao, P. Gong, L. Cai, K. M. C. Wong, *ACS Appl. Mater. Interfaces* **2019**, *11*, 8797–8806.
[60] I. Maisuls, T. M. Kirse, A. Hepp, J. Kösters, E. Wolcan, C. A. Strassert, *Inorg. Chem.* **2022**, *61*, 13775–13791.
[61] A. M. Potocny, J. J. Teesdale, A. Marangoz, G. P. A. Yap, J. Rosenthal, *Inorg. Chem.* **2019**, *58*, 5042–5050.
[62] K. Choroba, M. Penkala, J. Palion-Gazda, E. Malicka, B. Machura, *Inorg. Chem.* **2023**, *62*, 19256–19269.
[63] F. Ragone, H. H. M. Saavedra, P. M. D. Gara, G. T. Ruiz, E. Wolcan, *J. Phys. Chem. A* **2013**, *117*, 4428–4435.
[64] M. Małecka, A. Szlapa-Kula, A. M. Maron, P. Ledwon, M. Siwy, E. Schab-Balcerzak, K. Sulowska, S. Mackowski, K. Erfurt, B. Machura, *Inorg. Chem.* **2022**, *61*, 15070–15084.
[65] T. M. Kirse, I. Maisuls, M. V. Cappellari, E. Niehaves, J. Kösters, A. Hepp, U. Karst, E. Wolcan, C. A. Strassert, *Inorg. Chem.* **2024**, *63*, 4132–4151.
[66] Z. Y. Pan, D. H. Cai, L. He, *Dalt. Trans.* **2020**, *49*, 11583–11590.
[67] A. Acosta, J. Antipán, M. Fernández, G. Prado, C. Sandoval-Altamirano, G. Günther, I. Gutiérrez-Urrutia, I. Poblete-Castro, A. Vega, N. Pizarro, *RSC Adv.* **2021**, *11*, 31959–31966.
[68] A. Leonidova, V. Pierroz, R. Rubbiani, J. Heier, S. Ferrari, G. Gasser, *Dalt. Trans.* **2014**, *43*, 4287–4294.
[69] N. Manav, P. E. Kesavan, M. Ishida, S. Mori, Y. Yasutake, S. Fukatsu, H. Furuta, I. Gupta, *Dalt. Trans.* **2019**, *48*, 2467–2478.
[70] X. Yi, J. Zhao, J. Sun, S. Guo, H. Zhang, *Dalt. Trans.* **2013**, *42*, 2062–2074.
[71] S. H. Yu, M. Patra, S. Ferrari, P. Ramirez Garcia, N. A. Veldhuis, L. M. Kaminskas, B. Graham, J. F. Quinn, M. R. Whittaker, G. Gasser, T. P. Davis, *J. Mater. Chem. B* **2018**, *6*, 7805–7810.
[72] W. W. Feng, B. F. Liang, B. H. Chen, Q. Y. Liu, Z. Y. Pan, Y. J. Liu, L. He, *Dye. Pigment.* **2023**, *211*, 111077.
[73] F. Ragone, J. G. Yañuk, F. M. Cabrerizo, E. Prieto, E. Wolcan, G. T. Ruiz, *J. Inorg. Biochem.* **2024**, *252*. DOI: 10.1016/j.jinorgbio.2023.112471.
[74] X. R. Ma, J. J. Lu, B. Huang, X. Y. Lu, R. T. Li, R. R. Ye, *J. Inorg. Biochem.* **2023**, *240*, 112090.
[75] F. Jalilehvand, V. Brunskill, T. S. B. Trung, I. Lopetegui-Gonzalez, C. S. Shemanko, B. S. Gelfand, J. Bin Lin, *J. Inorg. Biochem.* **2023**, *240*, 112092.
[76] Y. Wang, P. S. Felder, P. Mesdom, O. Blacque, T. L. Mindt, G. Kevin Cariou, *ChemBioChem* **2023**, *24*, e202300467.
[77] H. K. Saeed, P. J. Jarman, S. Sreedharan, R. Mowll, A. J. Auty, A. A. P. Chauvet, C. G. W. Smythe, J. B. de la Serna, J. A. Thomas, *Chem. A Eur. J.* **2023**, *29*, 1–6.
[78] G. Mion, T. Gianferrara, A. Bergamo, G. Gasser, V. Pierroz, R. Rubbiani, R. Vilar, A. Leczkowska, E. Alessio, *ChemMedChem* **2015**, *10*, 1901–1914.
[79] A. Kastl, S. Dieckmann, K. Wahler, T. Vçlker, L. Kastl, A. L. Merkel, A. Vultur, B. Shannan, K. Harms, M. Ocker, W. J. Parak, M. Herlyn, E. Meggers, *ChemMedChem* **2013**, *8*, 924–927.
[80] N. Tyagi, N. Kaur, S. C. Sahoo, P. Venugopalan, *Appl Organomet. Chem.* **2022**, *36*, e6494.
[81] T. Gianferrara, C. Spagnul, R. Alberto, G. Gasser, S. Ferrari, V. Pierroz, A. Bergamo, E. Alessio, *ChemMedChem* **2014**, *9*, 1231–1237.
[82] A. M. Mansour, *Eur. J. Inorg. Chem.* **2018**, *2018*(44), 4805–4811.
[83] B. Kar, P. Paira, *Dalt. Trans.* **2022**, *51*, 15686–15695.
[84] M. J. Frisch, G. W. Trucks, H. B. Schlegel, G. E. Scuseria, M. A. Robb, J. R. Cheeseman, G. Scalmani, V. Barone, G. A. Petersson, H. Nakatsuji, X. Li, M. Caricato, A. Marenich, J. Bloino, B. G. Janesko, R. Gomperts, B. Mennucci, H. P. Hratchian, J. V. Ortiz, A. F. Izmaylov, J. L. Sonnenberg, D. Williams-Young, F. Ding, F. Lipparini, F. Egidi, J. Goings, B. Peng, A. Petrone, T. Henderson, D. Ranasinghe, V. G. Zakrzewski, J. Gao, N. Rega, G. Zheng, W. Liang, M. Hada, M. Ehara, K. Toyota, R. Fukuda, J. Hasegawa, M. Ishida, T. Nakajima, Y. Honda, O. Kitao, H. Nakai, T. Vreven, K. Throssell, J. A. Montgomery, Jr., J. E. Peralta, F. Ogliaro, M. Bearpark, J. J. Heyd, E. Brothers, K. N. Kudin, V. N. Staroverov, T. Keith, R. Kobayashi, J. Normand, K. Raghavachari, A. Rendell, J. C. Burant, S. S. Iyengar, J. Tomasi, M. Cossi, J. M. Millam, M. Klene, C. Adamo, R. Cammi, J. W. Ochterski, R. L. Martin, K. Morokuma, O. Farkas, J. B. Foresman, D. J. Fox, *Gaussian 09, Revision A.02*, Gaussian, Inc., Wallingford CT **2016**.
[85] M. Pal, D. Musib, A. J. Zade, N. Chowdhury, M. Roy, *ChemistrySelect* **2021**, *6*, 7429–7435.
[86] M. Pal, D. Musib, M. Roy, *New J. Chem.* **2021**, *45*, 1924–1933.
[87] G. M. Morris, R. Huey, W. Lindstrom, M. F. Sanner, R. K. Belew, D. S. Goodsell, A. J. Olson, *J. Comput. Chem.* **2009**, *30*, 2785–2791.
[88] H. R. Drew, R. M. Wing, T. Takano, C. Broka, S. Tanaka, K. Itakura, R. E. Dickerson, *Proc. Natl. Acad. Sci.* **1981**, *78*, 2179–2183.
[89] S. Sugio, A. Kashima, S. Mochizuki, M. Noda, K. Kobayashi, *Protein Eng.* **1999**, *12*, 439–446.
[90] BIOVIA, *Dassault Systèmes, Discovery Studio Visualizer 09*, Dassault Systèmes, San Diego **2020**.
[91] Desmond Molecular Dynamics System, D. E. Shaw Research, New York, *Maestro-Desmond Interoperability Tools*, Schrödinger, New York **2023**.

Manuscript received: May 1, 2024
Accepted manuscript online: September 13, 2024
Version of record online: November 5, 2024